d/Collection

Master's Thesis of Engineering

Synthesis and Multiferroic Properties of High-Purity CoFe$_2$O$_4$-BiFeO$_3$ Nanocomposites

고순도 CoFe$_2$O$_4$-BiFeO$_3$ 나노복합소재의 합성과 다강체 특성

February 2021

Graduate School of Engineering

Seoul National University

Materials Science and Engineering Major

Anindityo Nugra Arifiadi

Synthesis and Multiferroic Properties of High-Purity CoFe$_2$O$_4$-BiFeO$_3$ Nanocomposites

지도교수 김 상 국

이 논문을 공학석사 학위논문으로 제출함

2021년 02월

서울대학교 대학원

공과대학 재료공학부

Anindityo Nugra Arifiadi

Anindityo Nugra Arifiadi 의 공학석사

학위논문을 인준함

2021년 02월

위 원 장 _____ 홍 성 현 _____

부위원장 _____ 김 상 국 _____

위　　원 _____ 김 미 영 _____

Abstract

Anindityo Nugra Arifiadi

Department of Materials Science and Engineering

The Graduate School

Seoul National University

$CoFe_2O_4$−$BiFeO_3$ (CFO−BFO) nanocomposites of three different molar ratios (CFO:BFO = 2:2, 1.5:2, and 1:2) were synthesized by a combination hydrothermal/citric acid sol−gel method. This methodology allowed us to synthesize high−purity crystalline nanocomposites at a lower calcination temperature of 450°C. Transmission electron microscopy (TEM) images revealed that the CFO and BFO nanocrystals are inter−embedded in each other. Room−temperature magnetic characterizations showed that the sintered sample of the 2:2 ratio had a high magnetization value of 40.5 emu/g at 20 kOe. The magnetization and coercivity values indicated that the presence of dipolar interaction between CFO and BFO. The electric−polarization change (ΔP) was estimated to be ~295 μC/m^2 at a magnetic−field strength of ~30 kOe at room temperature, although the polarization−electric field (P−E) loop

measurements indicated that all of the samples manifested leaky behavior. The results presented herein offer a means of reliable magnetic–field control of electric polarization in high–purity multiferroic CFO–BFO nanocomposites.

Table of Contents

List of Figures

List of Tables

Chapter 1. Introduction

Chapter 1 presents the introduction to this thesis in two sections. The first section explains the motivation and background of this research and the second section presents the organization of this thesis.

1.1. Motivation and Background

Multiferroic materials have been the focus of many studies due to their promising applications in spintronic devices [1−3], catalysis [4, 5], and biomedicine [6, 7]. In this regard, $BiFeO_3$ (BFO) with its room−temperature antiferromagnetic (T_N ~ 643 K) and ferroelectric (T_C ~ 1,103 K) orderings has been considered to be the most promising multiferroic material [8, 9]. At the unit−cell level, BFO has a G−type antiferromagnetic ordering along its $[111]_c$ or $[001]_h$ axis in the distorted rhombohedral (*R3c*) structure, which distortion results in non−zero magnetization at this level. Superimposed on this atomic−scale ordering, BFO has a cycloidal spin configuration with a periodicity of 62 nm along its $[110]_h$ axis [10−12]. Concerning the ferroelectric ordering, one of its origins is the distortion from an ideal perovskite structure, resulting in antiferrodistortion (AFD), which causes rotation of the oxygen octahedra surrounding Fe^{3+} ions,

displacing both them and the O^{2-} ions from their original positions [13, 14].

Practical applications of the magnetoelectric effect in BFO, however, have been limited due to BFO's weak response to magnetic fields [15]. Thus, several strategies to enhance the magnetic response of BFO have been employed: breaking its cycloidal spin structure through size reduction below 62 nm [16, 17], introducing a dopant(s) [18−20], and/or incorporating spinel ferrites to form nanocomposites [21, 22]. Among those methods, the incorporation of spinel ferrites results in the highest enhancement of ferromagnetic behavior. Earlier studies of $CoFe_2O_4−BiFeO_3$ (CFO−BFO) nanocomposites have shown the existence of magnetoelectric coupling arising from a strain transfer from magnetostrictive CFO to piezoelectric BFO in samples prepared using either the sol−gel [22−24] or dip−coating method [25].

In quantifying the magnetoelectric coupling phenomenon, previous reports have utilized different property measurements, including changes in magnetoelectric coupling coefficient, dielectric property, or electrical polarization. The latest method − i.e., measuring changes in electrical polarization upon the application of

magnetic fields – allows for more in-depth measurements. However, the results of previous research using this method were obtained from Mn-doped BFO nanocomposites containing impurity phases and included only limited details on the magnetoelectric coupling measurements [23]. Therefore, as an effort to better quantify the electrical polarization upon the application of magnetic fields, we report herein a more comprehensive magnetoelectric property measurement of high-purity CFO-BFO nanocomposites. The high-purity nanocomposites were obtained by means of a modified version of the sol-gel method. Furthermore, in addition to the magnetoelectric property measurement, we also carried out experimental measurements of the magnetic and electrical properties.

1.2. Organization of the Thesis

The thesis is organized as follows:

Chapter 2 provides a review of multiferroicity and magnetoelectricity, properties of BFO and CFO, and the bottom-up synthesis methods of nanocrystals.

Chapter 3 covers the nanocomposite synthesis and characterization methods.

Chapter 4 presents the results showing the multiferroic and magnetoelectric property of CFO-BFO nanocomposites and their corresponding discussions.

Chapter 5 concludes the thesis. The obtained results from the three previous chapters are summarized in this chapter.

Chapter 2. Literature Review

Chapter 2 offers a brief review of the physical phenomena being studied in this thesis (multiferroicity and magnetoelectricity), the properties of BFO and CFO, and bottom-up synthesis methods of nanocrystals.

2.1. Multiferroic and Magnetoelectric Materials

Magnetoelectric materials are a type of multiferroic materials exhibiting a coupling of magnetic and electric properties. In this subchapter, the two physical phenomena contributing to multiferroicity – ferromagnetism and ferroelectricity – and magnetoelectric coupling will be reviewed.

2.1.1. Ferro- and Ferrimagnetism

Magnetism in materials is a physical phenomenon arising from electron orbiting a nucleus and spinning on its axis producing an orbital and spin magnetic moment, respectively. When an external magnetic field is applied to a material, this magnetic moment would align with the external field, resulting in the magnetization of the material. In many crystalline solids, however, the electrons' orbit is coupled rather strongly to the crystal lattice, thus when an external

magnetic field is applied, only the spins – which are loosely bounded to the lattice – will follow the orientation of the applied field. The result is that the material's magnetic moment arising only from electron spins [26].

The electron spins of two atoms interact with each other contributing to the total energy of the solid according to the Heisenberg model,

$$E_{ex} = -2J_{ex} \, \mathbf{S_i} \cdot \mathbf{S_j} = -2J_{ex}S_iS_j cos\theta \qquad (\text{II}.1)$$

where E_{ex} is the exchange energy, J_{ex} is the exchange integral, S_i and S_j are the spin angular momentum of electrons in atom i and j, respectively, and θ is the angle between the two spins. Depending on the atomic characteristics, J_{ex} can have a positive or negative value, when it is positive, the lowest E_{ex} can be achieved when the spins are parallel $(cos\theta = 1)$ to each other, resulting in ferromagnetism. Conversely, when J_{ex} is negative, the spins will arrange antiparallel to each other and the material will exhibit antiferromagnetism. J_{ex} is a function of temperature, the temperature above which magnetic ordering is lost is called the Currie (T_C) temperature for ferro and ferromagnetic materials and Neel (T_N) temperature for antiferromagnetic materials [26].

In antiferromagnetic oxide materials, the spin interaction occurs indirectly, due to the large distance between the metal ions, through a phenomenon called superexchange facilitated by oxygen ions illustrated in Figure 1. In this phenomenon, oxygen ions with fully filled outer shells play an important role in determining the spin direction of the metal ion. In a symmetric exchange, metal ion A with an up spin will pair itself with the down spin of the oxygen ion. The other electron in the oxygen shell must have an opposing spin – up spin – and this up spin will force metal ion B to have a down spin. This opposing spin of the two metal ions causes antiferromagnetism in solids. On the other hand, in asymmetric superexchange, a slight deviation exists due to the Dzyaloshinskii–Moriya interaction (DMI), causing the spins to be not completely antiparallel to each other [26–28].

When the two metal ions have a symmetric exchange interaction, and a different magnetic moment, another type of magnetism called ferrimagnetism arises. The moment imbalance causes the system to have a net magnetic moment, thereby causing a phenomenon similar to ferrimagnetism [26].
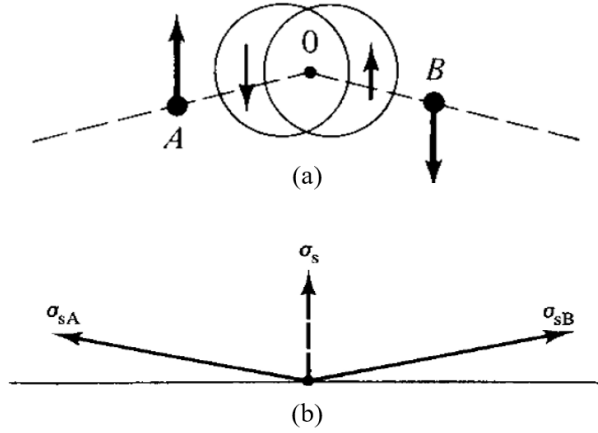
Figure 1. Illustration of (a) symmetric and (b) asymmetric

superexchange [26].

2.1.2. Ferroelectricity

Ferroelectricity is a term used as an analog to ferromagnetism, given to materials exhibiting spontaneous polarization even in the absence of an electric field. Ferroelectricity occurs only below a certain temperature called the Currie temperature (T_C) and it originates from the displacement of ions composing non-centrosymmetric crystals illustrated in Figure 2(a). The technological applications of ferroelectric materials arise from the polarizability of these materials by applying an electric field [29].

(a) BaTiO₃ tetragonal structure below 130 °C

(b) BaTiO₃ crystal under stress along y
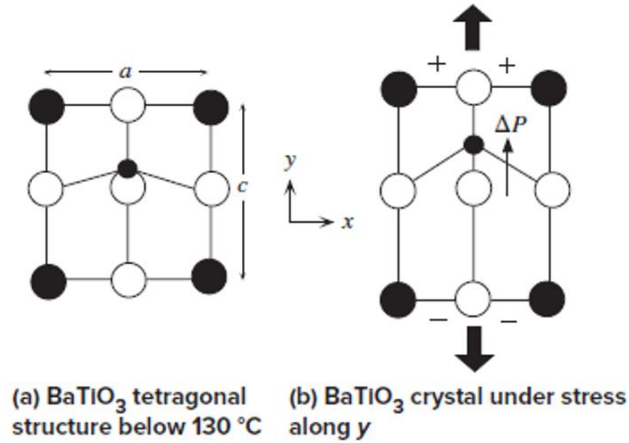
Figure 2. Illustration of (a)ferro- and (b)piezoelectricity in BaTiO3.

All ferroelectric materials also possess another property called piezoelectricity – the formation of electric polarization due to applied stress – yet not all piezoelectrics are ferroelectrics. Piezoelectricity is illustrated in Figure 2, it is shown that when stress is applied in y-direction, Ti^{4+} atom (black) is displaced, O^{2-} atom (white) is not. It is from this displacement that the polarization of the crystal is changed by ΔP [29].

2.1.3. Magnetoelectric Coupling

Magnetoelectrics refers to a class of materials exhibiting a coupling between their magnetic and electric properties. A single-phase magnetoelectric material can either be a multiferroic or non-multiferroic material as illustrated by the blue shades in Figure 3. In

other words, magnetoelectric coupling can occur in materials exhibiting ferromagnetism and ferroelectricity (red and blue region) or in magnetically (electrically) polarizable materials not exhibiting the aforementioned ferroic behaviors - paramagnetism (paraelectricity). In magnetoelectric materials, when a magnetic (electric) field is applied, electrical polarization (magnetization) will be induced. When this magnetoelectric coupling occurs in multiferroic materials, a novel memory device exploiting the benefits, while avoiding the drawbacks, of ferroelectric random access memory (FeRAM) and magnetic data storage may be created [30].
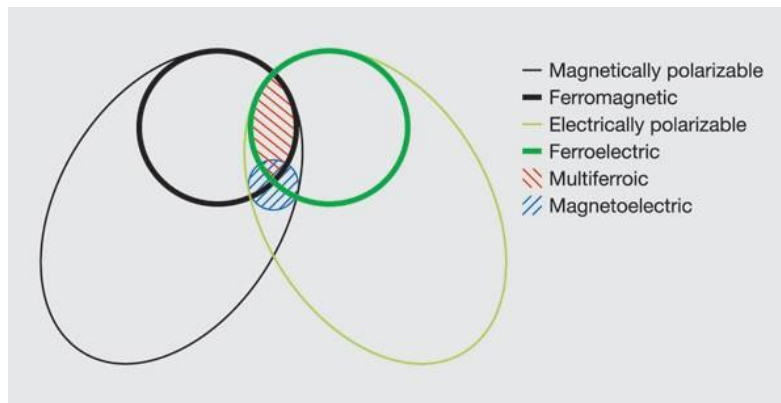
Figure 3. Classification of multiferroic and magnetoelectric

materials [30].

In addition to the single-phase materials previously explained, the magnetoelectric coupling can also be observed in multiphase materials. One strategy to engineer multiphase magnetoelectric

10

multiferroic materials is to introduce an indirect coupling, via strain, between the ferroelectric and ferromagnetic phases. The magnetoelectric coupling will arise as a result of strain transfer between magnetostrictive ferromagnetic and piezoelectric materials [30, 31].

2.2. Two-phase System

In general, there are two kinds of structure in the two-phase system – particle composite and thin-film heterostructures [30]. This section will present an overview of the former, a summary of $BiFeO_3$ (BFO) and $CoFe_2O_4$ (CFO) properties, and the methods of synthesizing the aforementioned materials.

2.2.1. Nanocomposite and Core-Shell Heterostructure

Nanocomposite is a type of particle composite system where one or both phases in the system are in the nanoscale regime. With this reduced dimensionality, nanocomposites are expected to show an enhanced magnetoelectric coupling due to the increased surface area thus enhanced strain transfer [31, 32]. To enhance the coupling even further, one can also engineer the nanocomposite structure into a core-shell heterostructure with an even larger interfacial area, facilitating the strain transfer [33, 34].

2.2.2. Properties of BiFeO₃

BFO is a peculiar material due to its ferroelectric and antiferromagnetic ordering at room temperature. This peculiarity originates from the instability of the ideal perovskite structure of BFO. Its structure transforms from the ideal perovskite structure (Figure 4(a)) to a rhombohedral distorted perovskite structure (Figure 5) with a symmetry group of R3c [11]. Ferroelectricity in BFO originates from the lone-pair mechanism, illustrated in Figure 5. Unbounded valence electrons of Bi^{3+} 6s orbital, not involved in sp hybridization, create a local dipole resulting in a spontaneous polarization of $\sim 100 \mu C\ cm^{-2}$ below the ferroelectric Curie temperature of 1,103K [35-37]. One additional source of electrical polarization is from antiferrodistortion (AFD); the rotation of the oxygen octahedra surrounding Fe^{3+} ions, displacing both O^{2-} and Fe^{3+} ions [13, 14] shown in Figure 5. This rhombohedral distortion also means that BFO crystal is non-centrosymmetric, thus enabling the formation of a net polarization due to the shifting of the center of mass when stress is applied i.e. piezoelectricity [29, 38].
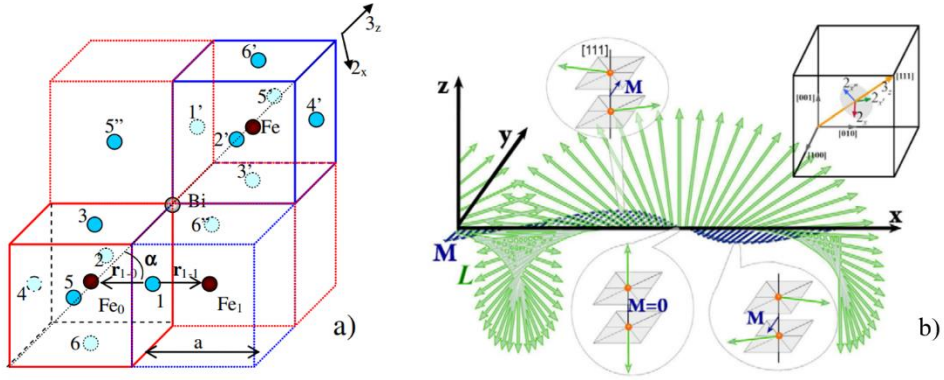
Figure 4. Illustration of (a) superexchange in an ideal perovskite structure and (b) the coexistence of spin cycloid (green arrows) and magnetization wave (blue arrows) [11, 39].
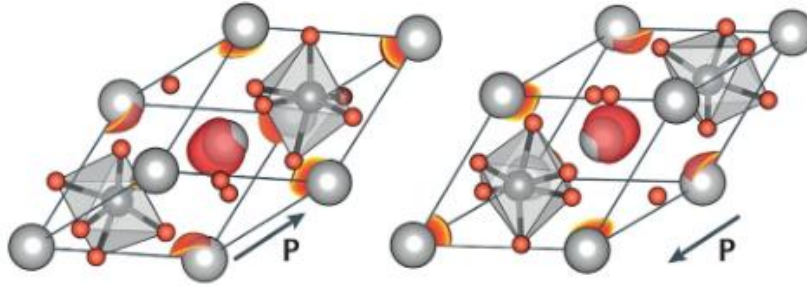
Figure 5. Illustration of lone pair mechanism in BFO (Bi^{3+}: big grey, O^{2-}: orange, Fe^{3+}: small grey) [36].

As for the antiferromagnetic ordering, it originates from the magnetization wave, having an average magnetization of zero throughout the spin cycloid (Figure 5(b)). The magnetization wave is formed due to the fluctuation of spin canting (M, blue arrows) depending on the orientation of the cycloidal antiferromagnetic vector

(green arrows) with respect to the [111] axis illustrated in the inset of Figure 5(b). These antiferromagnetic vectors arise from the asymmetric exchange interaction (DMI), facilitated by oxygen ions. The exchange energy per magnetic ion can be defined as the summation of exchange energy with the six nearest neighbors in the antiferromagnetic sub−lattice, expressed in (II.2) where V_{DM} is the Dzyaloshinskii−Moriya exchange energy, D_n is the Dzyaloshinskii vector, s_0 and s_n are the unit vector of the magnetic moments of Fe_0 and neighboring Fe_n, respectively. For Fe_0 ion in Figure 4(a), the exchange is facilitated by oxygen ions 1 to 6 [11].

$$V_{DM} = \frac{1}{2}\sum_{n}^{N=6}(D_n \cdot [s_0 \times s_n]) \qquad (II.2)$$

Dzyaloshinskii vector, D_n, is defined by the Keffer formula [40, 41],

$$D_n = V_0[r_{n-0} \times r_{n-n}], \qquad (II.3)$$

where V_0 is a constant, r_{n-0} and r_{n-n} are the position vector of magnetic ions directed from the nth oxygen ion to the nearest magnetic ions (see Figure 4(a)). In an ideal perovskite structure, D_n are all zero and thus V_{DM} is zero. On the other hand, the distortion of the perovskite structure of BFO results in a non−zero D_n, and thus DMI, forming antiferromagnetic vectors (green arrows, Figure 4(b)).

14

Finally, direct (converse) magnetoelectric coupling also exists in BFO, allowing for magnetic (electric) field control of electrical polarization (magnetization). Converse magnetoelectric coupling arises from the contribution of AFD to the r_{n-0} and r_{n-n}, used for the calculation of the Dzyaloshiinski vector in (II.3). An applied electric field can alter the polarization of BFO crystal by altering the AFD vector, thus changing the Dzyaloshiinski and antiferromagnetic vector. [11, 14] As for the converse magnetoelectric coupling, an applied magnetic field can alter the spin cycloid structure of BFO and thus change its electrical polarization [15, 39]. The spin cycloid wave vector (q_o) in BFO can be calculated using (II.4) obtained from the volume−averaged free−energy density $(\langle F \rangle)$ expressed in (II.5), where λ is the period of the cycloid, γ is the constant of inhomogenous magnetoelectric effect, P_z is the electric polarization along the z direction of BFO rhombohedra, A is the exchange stiffness, and K_{eff} is the anisotropy constant [39].

$$q = \frac{2\pi}{\lambda} = \frac{\gamma P_z}{2A} \tag{II.4}$$

$$\langle F \rangle = Aq^2 - (\gamma P_z)q - \frac{K_{eff}}{2} \tag{II.5}$$

An applied magnetic field may change K_{eff}, at low fields, the change is negligible and thus $\langle F \rangle$ does not change much. At high fields, however, K_{eff} can be significant compared to Aq^2 and therefore may alter $\langle F \rangle$ and q. Changes in q can modify the electric polarization of BFO averaged throughout the cycloid ($\langle \Delta P \rangle$) according to (II.6), where κ is the electric susceptibility of BFO.

$$\langle \Delta P \rangle = \frac{2\kappa Aq^2}{Pz} \tag{II.3}$$

Since different magnetic field directions alter q in different ways, $\langle \Delta P \rangle$ varies depending on the direction of the applied field [15, 39].

2.2.3. Properties of CoFe$_2$O$_4$

CFO is a type of magnetic ferrites with a spinel structure. Its oxygen ions are arranged in a face-centered cubic manner and its metallic ions occupy the spaces between them. The available spaces are divided into tetrahedral (A) sites and octahedral (B) sites shown in Figure 6(a) and (b), respectively. The position of A and B sites in a spinel unit cell are illustrated in Figure 6(d), which is a part of a spinel unit cell divided into eight octants shown in Figure 6(c).

16
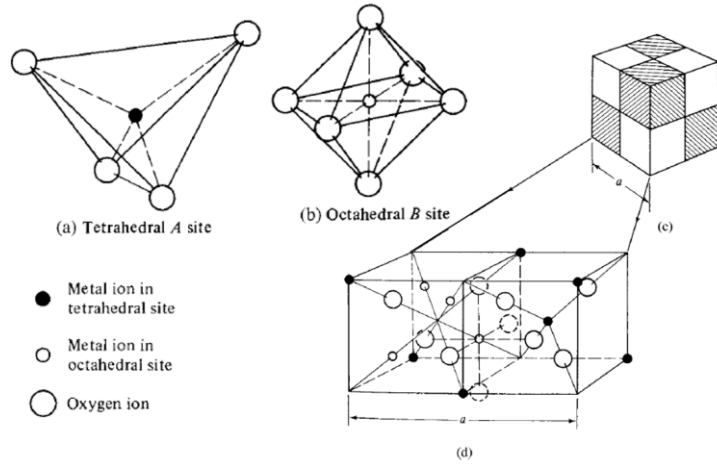
Figure 6. Crystal structure of a cubic ferrite [26].

In spinel ferrites, only one-eighth of the A sites and one-half of the B sites are occupied. Furthermore, in the case of CFO, despite the general chemical formula of AB_2O_4, not all A atoms are located in A sites and not all B atoms are located in B sites, resulting in a structure called the inverse spinel. Since the magnetic interaction within and without A and B sites are different, the cation mixing determines the magnetic property of spinel ferrites [26].

One important property of CFO utilized for magnetoelectric nanocomposite is its magnetostriction; the deformation of materials upon the application of a magnetic field. The origin of this deformation is spin-orbit coupling, causing a non-spherical distribution of electron cloud, illustrated in Figure 7. Depending on the magnetic

17

ordering and applied field, the materials will have different dimensions. For CFO in polycrystalline form, its magnetostriction constant λ_p is -110×10^6, the highest among spinel ferrites [26].
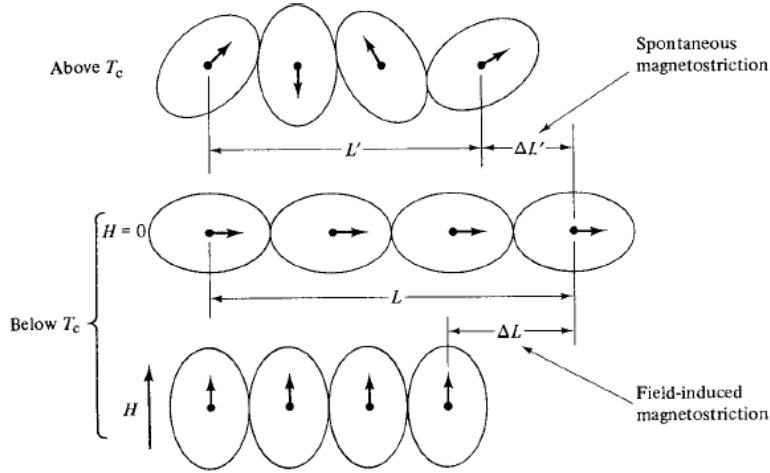
Figure 7. Illustration of magnetostriction [26].

2.2.4. Nanocrystals Synthesis

To synthesize an agglomerate or a core−shell nanocomposite, one needs to be able to synthesize nanocrystals of its constituent. This chapter will review the bottom−up approach of nanocrystals synthesis. The general principle of this approach is the nucleation of nanocrystals from its precursor and growth of nanocrystals. There are several methods to carry out this nucleation and growth process, each having different shape and size controllability. Figure 8 shows the TEM images of nanoparticles synthesized using the

18

organometallic thermal decomposition [42], solvothermal [43], hydrothermal [44], and sol-gel method [17].
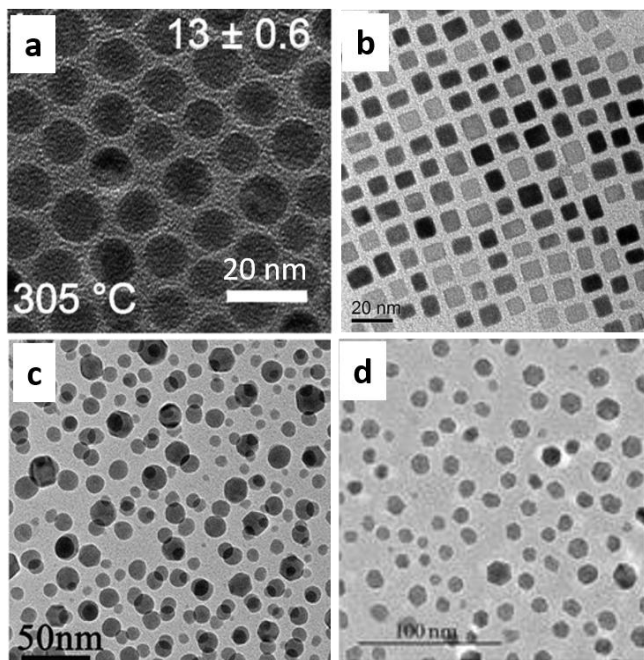
Figure 8. TEM images of (a) $CoFe_2O_4$, (b) $BaTiO_3$, and (c)-(d) $BiFeO_3$ nanoparticles synthesized using the (a) organometallic thermal decomposition, (b) solvothermal, (c) hydrothermal, and (d) sol-gel method [17, 42-44].

The organometallic thermal decomposition method offers the best precision for monodispersity and size control of nanocrystals, due to the separation of nucleation and growth process. Nanocrystals are nucleated homogeneously by heating up a solution of organic solvent, organometallic precursor, and surfactant in a controlled

manner, allowing for a quick increase of monomer concentration thus burst nucleation. Monodispersity obtained from this uniform nucleation is maintained by the presence of surfactant, prohibiting nanocrystal coalescence. Particle growth – which will determine the final particle size – can then be controlled by adjusting the aging time and temperature. [45]. Different types of compounds can be used as the organometallic precursor, yet the simplest precursors are metal−oleate complexes [42, 46].

The solvothermal method produces nanocrystals with good control of size and monodispersity, though not as precise as those produced by the organometallic thermal decomposition method. The solvothermal reaction is carried out in an autoclave, usually in a mixture of non−aqueous solvent and water. The mechanism of solvothermal reaction differs depending on the precursor and the solvent. An example of a solvothermal reaction mechanism is explained as follows. When NaOH solution is mixed with an organic solvent containing metal oleate precursors, the two will remain separated and form an interface. Nucleation occurs when the autoclave is heated above 100°C, forming water vapor that will move up through the organic solvent. Some hydroxide ions will be transported with the water vapor and react with the metal oleate

precursor. The reaction will produce metal hydroxide monomers and sodium oleate layer. It is in this layer where nucleation and growth occur [43, 47].

The hydrothermal method, unlike the previous two methods, is much simpler due to the use of water as the solvent. Yet this simplicity comes at the expense of monodispersity and size control. In this method, metal hydroxide precipitates are used as precursors. By heating the precipitate in a highly basic solution in a Teflon lined autoclave, metal hydroxide precipitates will react with hydroxide ions and form soluble metal hydroxide complexes. Once saturation is reached, these complexes will nucleate and form nanocrystals. However, the absence of stirring in the autoclave makes it difficult to maintain a homogenous solution condition, thus control of size and monodispersity is limited [44, 48, 49].

The sol–gel method is the most versatile method of synthesizing nanocrystals. Similar to the hydrothermal method, the simplicity of this method comes at the cost of monodispersity and size control. In the sol–gel method, a chelating agent e.g. citric acid is used to form metal citrate complexes, which will decompose when calcined. The decomposition is the origin of nanocrystals nucleation. To control the size of the nanocrystals, one can adjust the calcination

temperature or use different chelating agents. However, since calcination is carried out in static and dry conditions, it is often hard to avoid particle coalescence [17].

Chapter 3. Experimental Methods

This chapter explains the synthesis and characterization method of CFO−BFO nanocomposites. The materials used and the step by step procedure are described in the first part. The characterization devices and the characterization parameters are described in the second part.

3.1. Synthesis

Synthesis of the CFO−BFO nanocomposites was carried out in two steps using reagent−grade chemicals without further purification. First, CFO was synthesized and then coated with BFO precursor. To prepare the CFO nanocrystals, 4 mmol of $Co(NO_3)_2 \cdot 6H_2O$ and 8 mmol of $Fe(NO_3)_3 \cdot 9H_2O$ were dissolved in 40 mL of deionized (DI) water, and then 3.6 mL of 10M NaOH was added dropwise. Next, the mixture was stirred for 10 min and then transferred to a 70 mL Teflon−lined stainless steel autoclave to undergo hydrothermal treatment at 180° C for 15 h. Upon the completion of the treatment, the reactor was air−cooled and the reaction product was washed with DI water and ethanol before being dried in an oven at 90° C for 3 h.

To synthesize the nanocomposites, BFO precursor was prepared using the citric acid sol-gel method [17, 50]. Initially, 2 mmol of $Fe(NO_3)_3 \cdot 9H_2O$ and 2.2 mmol of $Bi(NO_3)_3 \cdot 5H_2O$ were mixed with 8 mmol citric acid in 20 mL DI water in a round-bottom flask. Upon addition of 3 mL concentrated (70%) nitric acid under stirring at 500 rpm, the solution was turned to a light yellow color and then was heated to 140° C using a heating mantle. Subsequently, once the solution volume was reduced to ~10 mL and the solution color became orange after ~1.5 h of stirring at 140° C, a certain amount of CFO nanocrystals was added. This mixture was further stirred for 45 min to evaporate all the liquid and then dried in an oven at 150° C for 1 h. The dried precursor was then calcined in a furnace for 1 h at 450° C at a heating rate of 5° C/min. After being calcined, the powder was air-cooled, washed in 20 mL 0.5 M HNO_3 for 15 min, and then washed with DI water and ethanol before being dried in an oven at 90° C for 3 h. Three different amounts of CFO nanocrystals, 2, 1.5, and 1 mmol, were added to impart different molar ratios to the nanocomposites, namely CB22, CB152, and CB12, respectively. For measurement of the magnetic, ferroelectric, and magnetoelectric properties, the powders were pelletized (d = 10 mm, t = ~0.7 mm) with the help of 4% PVA and then sintered in air at

24

400° C for 2 h.

3.2. Characterizations

The crystal structures of the samples were investigated by powder X-ray diffraction measurements (XRD; Rigagu MiniFlex 500 X-ray diffractometer) with Cu-Kα radiation (λ = 1.5406 Å). Rietveld refinements of the measured diffraction patterns were performed using MAUD software (version 2.93) [51]. Transmission electron microscopy (TEM) images and electron diffraction patterns were taken using a Tecnai F20 TEM. For these characterizations, a small amount of nanocomposite powder was dispersed in ethanol and then drop cast on lacey carbon film on copper TEM grids. Magnetic hysteresis loops were measured using a vibrating sample magnetometer (VSM, Lake Shore VSM-7420). For electrical property measurements, we shaped the sintered pellet samples into thin plates having a thickness of ~0.15 mm and an area of ~3 mm^2. Electrodes were made by coating both sides of the thin plates with silver epoxy. We measured electric polarization (P) versus electric field (E) loops using the Sawyer-Tower circuit [52]. The magnetic-field-dependent currents were also measured using an electrometer (Keithley 617). We used a 9T PPMS™ (Quantum Design) to apply

strong magnetic fields at room temperature. Before the measurements, the samples were poled with a positive or negative electric field, $E_p = \pm 100$ V, under a positive or negative magnetic field, $H = \pm 50$ kOe. The applied electric fields were removed after 5 min poling and the samples were left for 30 min to reduce the leakage current. Finally, the electrical current was measured under a sweeping magnetic field at a rate of $dH/dt = \pm 100$ Oe/s, and electric polarization was obtained by integrating the current with respect to the measurement time [53].

Chapter 4. Results and Discussion

Chapter 4 presents the characterization results of CFO-BFO nanocomposites. Crystal structure and morphology, as well as magnetic, electric, and magnetoelectric property characterization results and their discussion are presented in the subchapters.

4.1. X-ray diffraction (XRD)

The XRD patterns and Rietveld refinements of the CFO-BFO nanocomposites and sintered CFO-BFO nanocomposites are shown in Figure 9 (also see Figure 10 for single-phase CFO and BFO powder samples), and the structural parameters estimated from the Rietveld refinements are given in Tables 1 and 2. For the sintered samples, pellets were first pulverized before their XRD measurements. All of the samples showed high crystallinities. The diffraction patterns of the CFO and BFO powders were well fitted to two different space groups, $Fd-3m$ and $R3c$, respectively. We note that although some of the XRD patterns of the nanocomposite (Figures 9(b), 9(c), 9(e), 9(f)) showed small amounts of impurities around ~29°, the phase purity of the nanocomposites was much higher than those synthesized previously [23, 54]. We even managed to obtain this phase purity at a lower calcination temperature of 450°

C [23, 24, 54]. Nevertheless, we were unable to estimate the weight percentage of this impurity phase using Rietveld refinement due to the small amounts of the impurities.

The high purity of our samples can be attributed to the higher amount of Bi^{3+} precursor used in the sol—gel synthesis of BFO. This Bi^{3+}—rich environment compensated for the excess Fe^{3+} in the solution due to the dissolution of CFO nanocrystals during the sol—gel synthesis of BFO, shifted the Bi—Fe equilibrium, and thus promoted the formation of $Bi_{25}FeO_{40}$ instead of $Bi_2Fe_4O_9$ (see Supplementary Figures 11(a) and 11(b)). Unlike $Bi_2Fe_4O_9$, $Bi_{25}FeO_{40}$ is known to be easily dissolvable in dilute HNO_3 solution [55]. This washing step, however, changed the CFO—BFO molar ratio in the final product. The Rietveld refinement of unwashed CB22 (see Figure 12 and Table 3) showed that the initial molar ratio of CFO—BFO was close to 1:1. After washing, though, the value was shifted to ~2:1, indicating that BFO dissolves more easily in HNO_3.

The structural parameters summarized in Table 1 indicate that the lattice constants of CFO and BFO were consistent for all of the samples and that the goodness of fit (S) was close to 1. The crystallite size of BFO in the nanocomposite samples increased with

decreasing CFO content (Figure 13(a)), which indicates that the CFO nanocrystals can act as heterogeneous nucleation sites for the Bi—Fe citrate precursor; accordingly, a higher amount of CFO leads to an increase of nucleation sites, consuming more precursors for the nucleation, and also preventing the nucleated crystals from growing to larger crystals. The occupancy of both the tetrahedral and octahedral sites, as shown in Table 2, revealed that the CFO nanocrystals and the CFO phase within the nanocomposites have a mixture of normal and inverse spinel structures, though the inverse spinel structure is more dominant (Figure 13(b)) since most of the Co^{2+} ions are located at the octahedral sites [56].
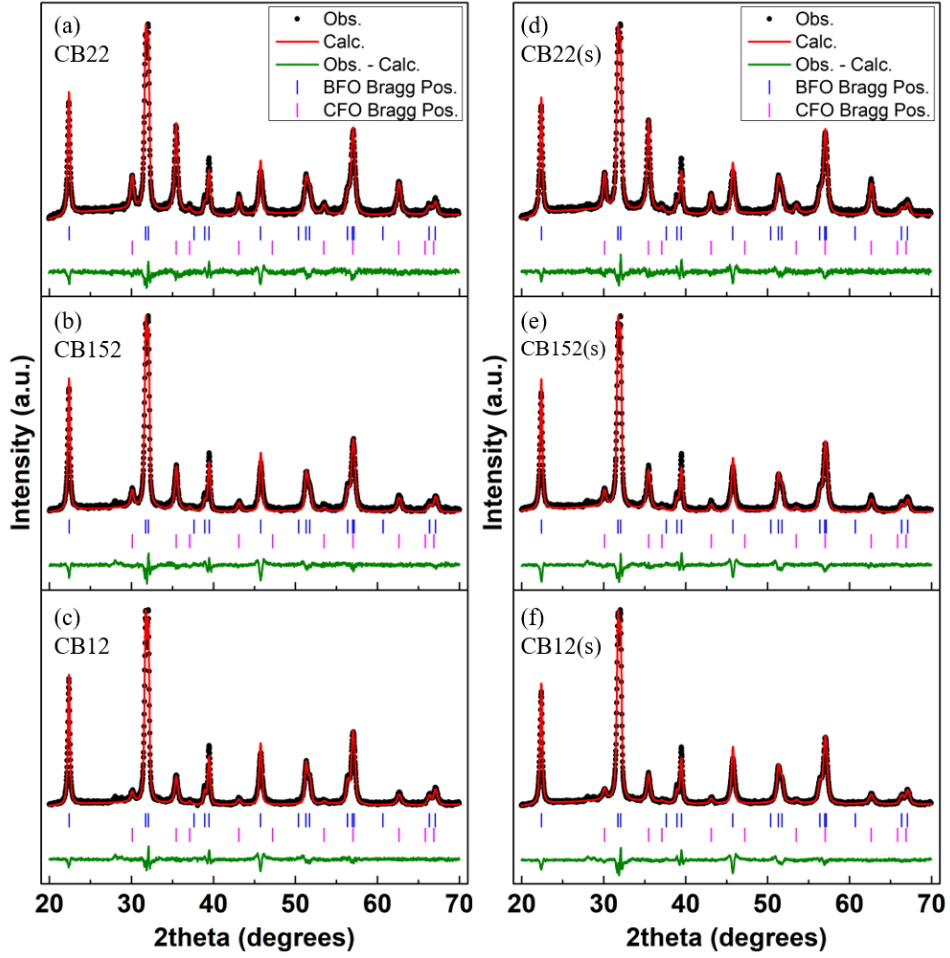
Figure 9. Measured XRD patterns and Rietveld refinements for (a)－ (c) CFO－BFO nanocomposites with indicated different CFO－BFO ratios, and (d)－(f) sintered CFO－BFO nanocomposites. The sign '(s)' indicates that the samples were sintered.
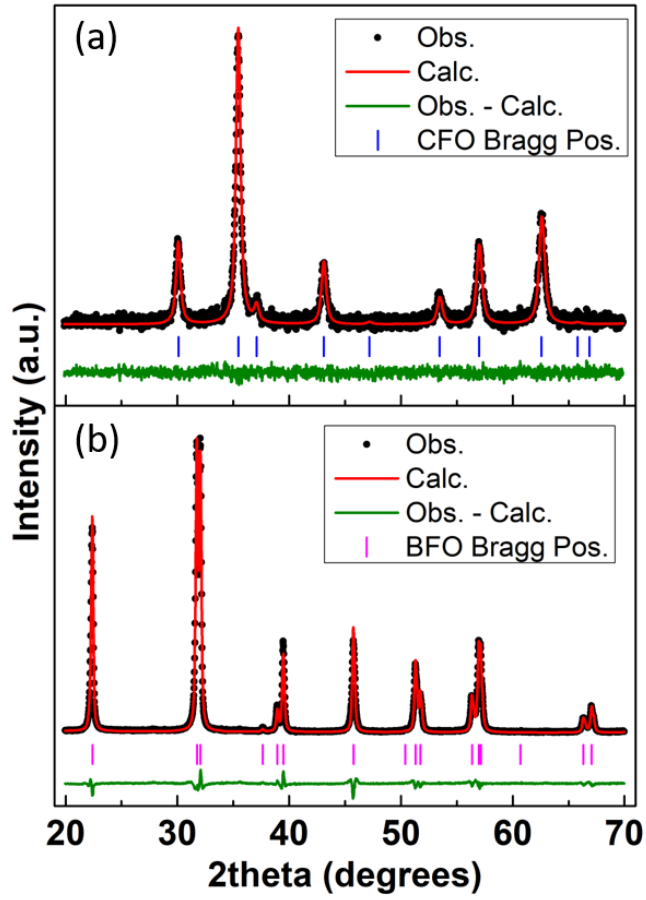
Figure 10. Measured XRD patterns and Rietveld refinements of single-phase (a) CFO and (b) BFO powder samples. Here, BFO nanocrystals were synthesized using an equimolar amount of Bi^{3+} and Fe^{3+} (2 mmol).
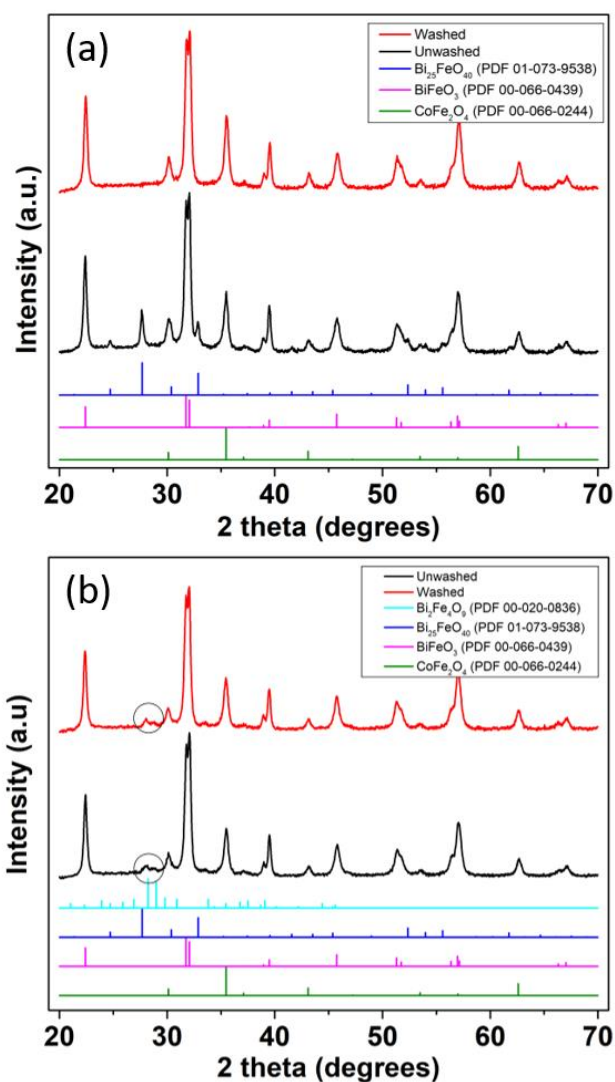
Figure 9. Comparison of measured XRD patterns for CB22 nanocomposites synthesized using (a) 2.2 mmol and (b) 2 mmol of Bi^{3+}, before (black) and after (red) HNO_3 washes. Note that the secondary phase ($Bi_{25}FeO_{40}$) was completely removed after washing in (a), but that $Bi_2Fe_4O_9$ remained even after HNO_3 washing in (b).
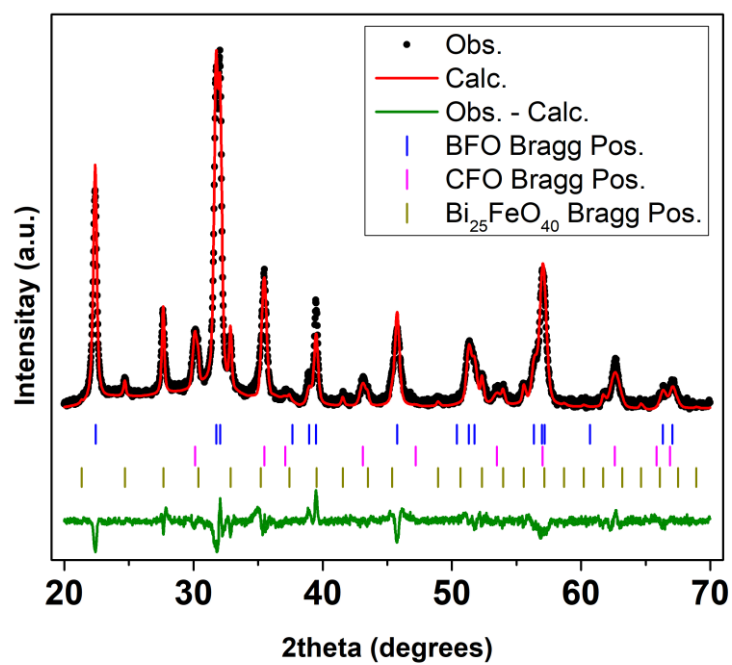
Figure 10. Measured XRD pattern and Rietveld refinement of

unwashed CB22 nanocomposite.

Table 1. Rietveld refinements of CFO, three different CFO−BFO nanocomposites, and their sintered samples. Here, a, b, and c are lattice constants, and S is the goodness of fitting.

Parameters	CFO	CB22		CB152		CB12	
		CFO	BFO	CFO	BFO	CFO	BFO
a (Å) b (Å)	8.3904(7)	8.3868(5)	5.5787(3)	8.3842(6)	5.5761(3)	8.3842(7)	5.5780(3)
c (Å)			13.867(1)		13.8606(9)		13.8652(9)
Crsyt. size (nm)	26.3(2)	30.5(4)	49.1(6)	29.8(4)	56.0(6)	27.4(9)	59.1(3)
Weight (%)	100	61	39(1)	45	55.0(5)	33	67(1)
S	0.88	1.16		1.54		1.54	

Parameters	BFO	CB22(s)		CB152(s)		CB12(s)	
		CFO	BFO	CFO	BFO	CFO	BFO
a (Å) b (Å)	5.5778(1)	8.3846(5)	5.5773(4)	8.3838(5)	5.5763(2)	8.3834(8)	5.5768(3)
c (Å)	13.8655(4)		13.863(1)		13.8611(8)		13.8615(9)
Crsyt. size (nm)	94.0(6)	30.3(3)	46.0(6)	26.6(5)	50.1(4)	28.0(4)	52.8(4)
Weight (%)	100	60	40(1)	44.7	55.3(9)	33	67(1)
S	2.01	1.28		1.74		1.79	
$\rho_{theoritical}$ (g/cm^3)		6.51		6.98		7.34	
$\rho_{measured}$ (g/cm^3)	-	3.62		3.3		3.53	
$\rho_{relative}$ (%)		50.39		47.29		48.06	

Table 2. Position and occupancy of Co^{2+}, Fe^{3+}, and $O2-$ ions in CFO, CB22(s), CB152(s), and CB12(s), as obtained from Rietveld refinements.

Site	Atom	CFO		CB22(s)		CB152(s)		CB12(s)	
		Coord. (x,y,z)	Occu-pancy	Coord. (x,y,z)	Occu-pancy	Coord. (x,y,z)	Occu-pancy	Coord. (x,y,z)	Occu-pancy
8a tetrahedral	Co1	0.125	0.255(6)	0.125	0.34(2)	0.125	0.26(5)	0.125	0.36(5)
	Fe1		0.746(6)		0.66(1)		0.72(6)		0.70(5)
16d octahedral	Co2	0.5	0.373(7)	0.5	0.37(1)	0.5	0.36(7)	0.5	0.33(3)
	Fe2		0.605(7)		0.65(1)		0.66(7)		0.63(3)
32e	O1	0.2510(7)	0.946(8)	0.2718(8)	1.00(4)	0.2734(8)	1.0(2)	0.270(2)	1.00(3)

Table 3. Compositions of unwashed and washed CB22 composites, as obtained from Rietveld refinements. The asterisk (*) sign indicates that the value was obtained through further calculation.

Parameters	CB22 unwashed			CB22 washed	
	CFO	BFO	$Bi_{25}FeO_{40}$	CFO	BFO
Weight (%)	44(2)	50	6	61	39(1)
S		1.64		1.16	
Mol (%)*	53.8	45.9	0.3	68	32
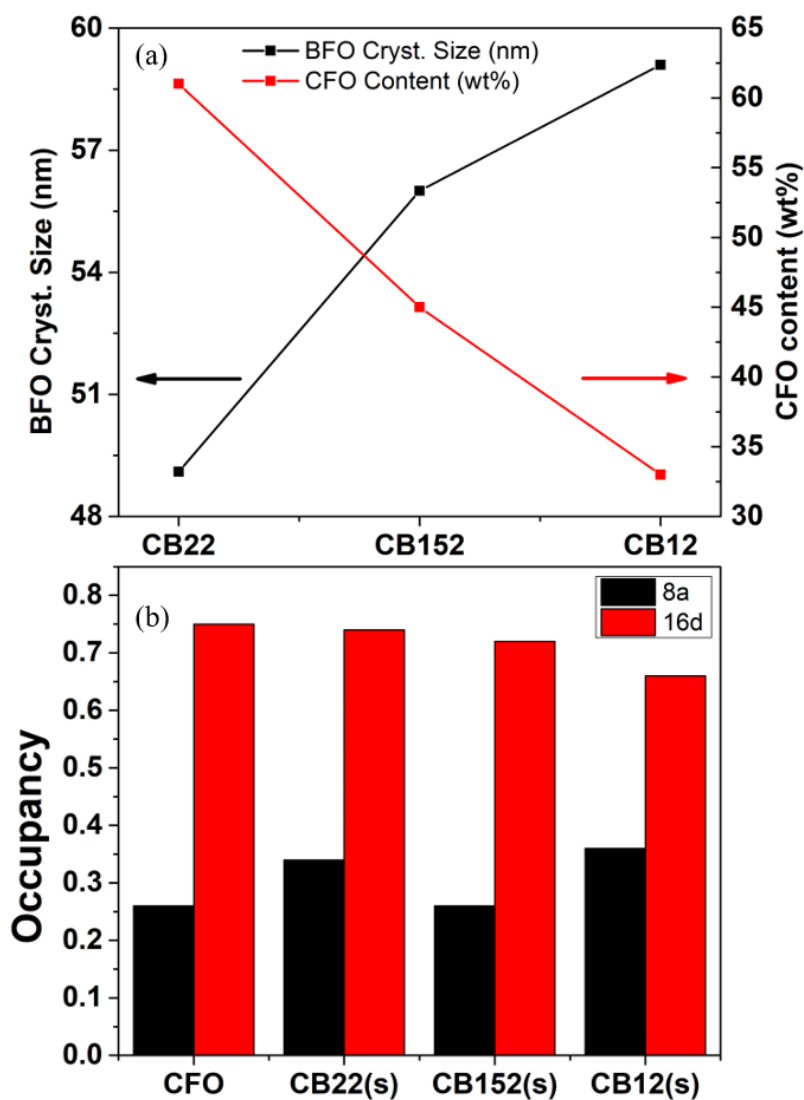
Figure 11. (a) Relationship between crystallite size and CFO content and (b) comparison of Co^{2+} occupancy in the tetrahedral and octahedral sites.

4.2. Transmission Electron Microscopy (TEM)

Bright-field and high-resolution (HR) TEM images for the CFO nanocrystals are shown in Figures 14(a) and 14(b), respectively. Agglomeration of the CFO nanocrystals, shown in Figures 14(a), is typical for hydrothermally synthesized nanocrystals, as reported in Ref. [57]. The average size of the nanocrystals was measured to about 22.5 nm, as shown in the size-distribution histogram (inset), which value is close to that obtained from the XRD analysis. The HR-TEM image of a selected CFO nanocrystal (Figures 14(b)) shows non-spherical shapes and well-defined lattice fringes. The distance between the fringes, marked in Figures 14(b), was measured to be 0.295 nm, corresponding to the (220) planes of CFO (see PDF 00-066-0244).

Figures 14(c), 14(e), and14(g) show bright-field TEM images of the agglomerated nanocomposites for three different samples, CB22, CB152, and CB12, respectively. The selected area electron diffraction (SAED) patterns shown in the corresponding insets corroborate the sample crystallinity determined by the XRD analysis. Furthermore, the indexing of the SAED patterns (PDF 00-066-0244 and PDF 00-066-0439) indicated the existence of

37

both the CFO and BFO nanocrystals in the agglomerates having sizes larger than 100 nm. By indexing the interplanar spacing of individual nanocrystals in Figures 14(d), 14(f), and 14(h), we found that the BFO phase crystallized separately from the CFO phase, forming inter-embedded CFO-BFO nanocrystals, instead of forming a core-shell structure. The inter-embedded structure of the nanocrystals, however, creates a sufficiently large area of interfaces, allowing CFO nanocrystals to induce a significant effect on the electrical properties of BFO upon the application of a magnetic field, as shown later in this paper and in Ref. [22].
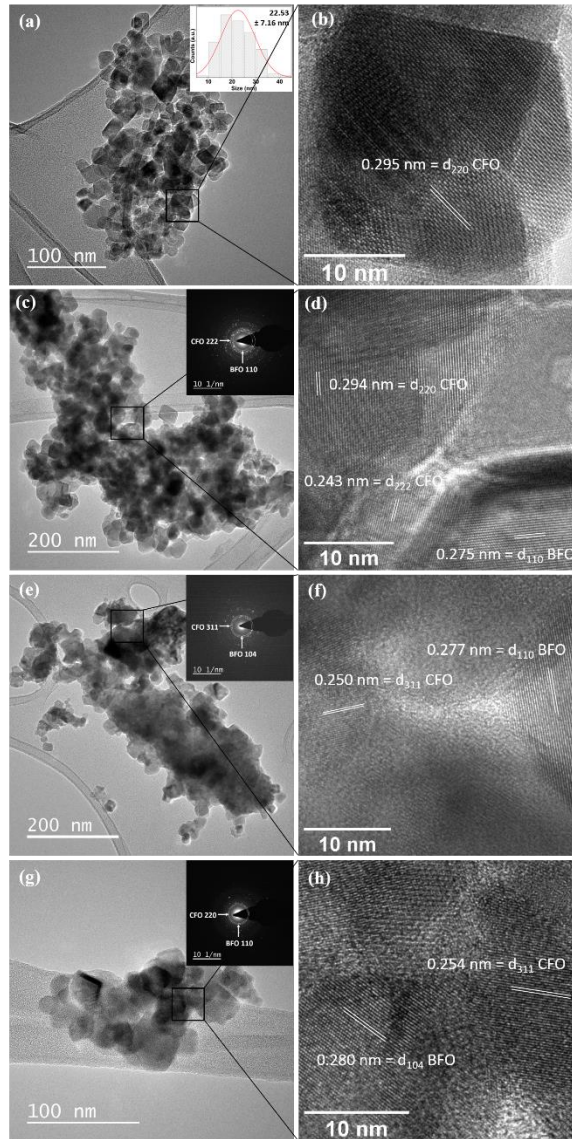
Figure 12. TEM morphology images (left column) and HR–TEM lattice images (right column) for (a) CFO nanocrystals, (b) CB22, (c) CB152, and (d) CB12. The inset in (a) shows the particle–size histogram of the CFO nanocrystals and the insets in (c), (e), and (g) show the SAED patterns of the corresponding nanocomposites.

4.3. Magnetic Properties

Magnetization hysteresis ($M-H$) loops measured at room temperature for the CFO and sintered CFO−BFO nanocomposites (samples CB22(s), CB152(s), CB12(s)) are shown in Figure 15. The $M-H$ loops do not show magnetization saturation even at 20 kOe, reflecting the presence of the ferromagnetic (FM) and paramagnetic/antiferromagnetic (PM/AFM) contributions to the loops. Therefore, to obtain the values of several magnetic parameters and to separate the FM and the PM/AFM parts of those $M-H$ loops, we fitted the $M-H$ curves using Eq. (IV.1) [18, 58, 59]:

$$M(H) = \frac{2M_s}{\pi}\tan^{-1}\left[\frac{H \pm H_c}{H_c}\tan\left(\frac{\pi S}{2}\right)\right] + \chi H \qquad (IV.1)$$

where M_s is the saturation magnetization, H_c is the coercivity, $S = M_r/M_s$ is the squareness of the hysteresis loop, and χ is the magnetic susceptibility. The first and second terms represent the FM and PM/AFM contributions, respectively. The overall fitting results and the FM and PM/AFM parts are shown in Figures 16(a)−16(d) and in the insets, respectively. The resultant fitting parameters, M_s, M_r, H_c, and χ, are given in Table 3.

For CFO, the magnetization did not fully saturate, as indicated

by the presence of the PM/AFM contribution (see Figure 16(a)) and the magnetization value was calculated to 71.6 emu/g at a sufficiently high field strength of 20 kOe. There seem to be two possible reasons for this non-saturation behavior. First, the inverse spinel structure of the sample, as indicated by Co^{2+} ions occupying the octahedral sites (see Table 2), can make the crystals highly anisotropic [60], and second, the random orientation distribution of the crystals makes it difficult for local magnetizations in the individual crystals to orient in the applied field direction. Such non-saturation behavior was also observed in the nanocomposite samples (Figures 16(b)-16(d) and Table 4). In the nanocomposite samples, the contribution of PM/AFM increased with the CFO content, which can be attributed to the coupling of the canted spins on the BFO surface with the ordered spins of CFO [61]. The non-saturation behavior of CFO nanocrystals could be extended to the surface spins of BFO, resulting in an increase of non-saturation contribution in proportion to the CFO content in the CFO-BFO composites.

Using the weight ratios estimated from the Rietveld refinements and the magnetization value of CFO, we determined the effect of CFO content on the magnetization values of the nanocomposites. The magnetization values were 43.7, 32.3, and 23.6

41

emu/g at 20 kOe for sample CB22(s), CB152(s) and CB12(s), respectively. The discrepancies between these values and the measured ones listed in Table 4 and shown in Figure 17(a) may indicate the presence of dipolar interaction between the CFO and BFO nanocrystals [22], as shown in Figures 14(d), 14(f), and 14(g). The dipolar interaction can also result in enhanced coercivity (H_c) of nanocomposites. In Table 4, it is shown that all of the samples possessed H_c values higher than that of CFO itself (864 Oe). Although the increased H_c may also have been caused by the larger crystallite size of the nanocomposites (Table 1), we noticed that the value H_c = 991 Oe for CB152(s) was 15% higher than that of CFO (864 Oe), despite having similar crystallite sizes (26.6 vs. 26.3 nm). The explanation behind such H_c enhancement is the coupling of the antiferromagnetic spin of BFO with the ferrimagnetic spin of CFO, resulting in an increase in energy for spin rotation [61, 62]. Finally, we found that H_c for the nanocomposites depends on the size of CFO crystallites (Figure 17(b)). Samples CB22(s), CB152(s), and CB12(s) had crystallite sizes of 30.3, 26.6, and 28.0 nm, respectively, showing H_c = 1106, 991, and 996 Oe, respectively. This observation is in agreement with previous reports wherein H_c increased with increasing crystallite size [63, 64].

42
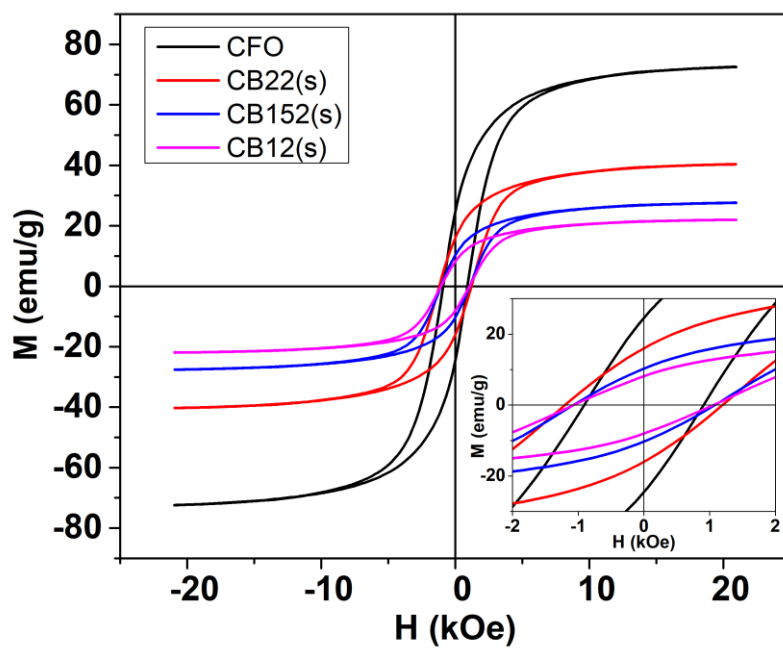
Figure 13. Comparison of $M{-}H$ loops for CFO nanocrystals and
sintered nanocomposites. The inset shows the corresponding
magnified loops in a low field range.
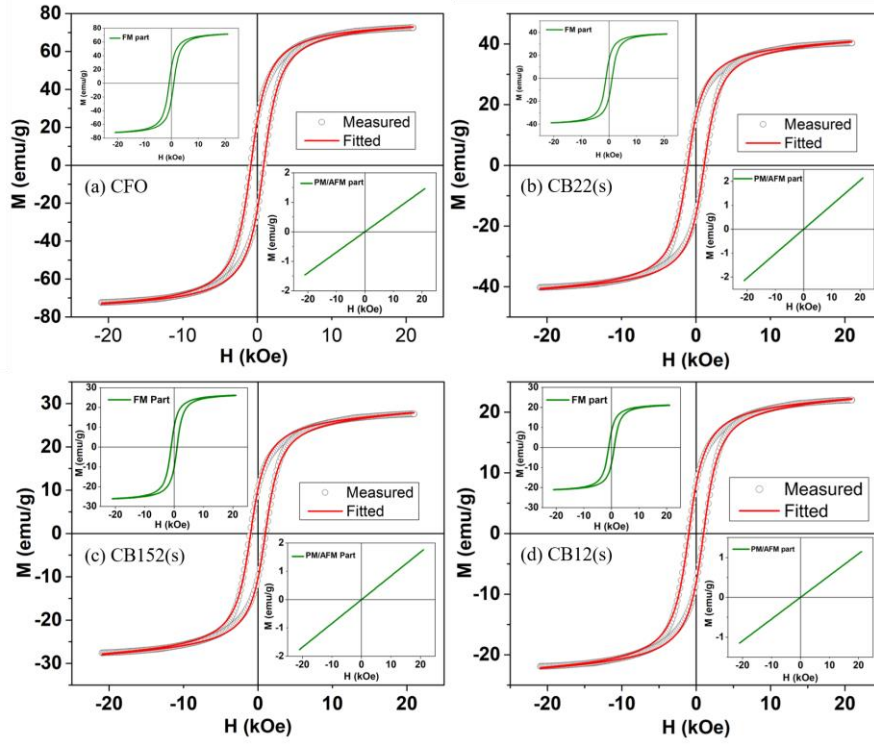
Figure 14. Fitting results for Eq. (IV.1) and measured $M-H$ loops for CFO nanocrystals, CB22(s), CB152(s), and CB12(s). The open circles and red solid lines indicate the measured data and fitting results, respectively. The insets show the fitted loops for the FM (left upper) and PM/AFM (right lower) contributions, respectively.
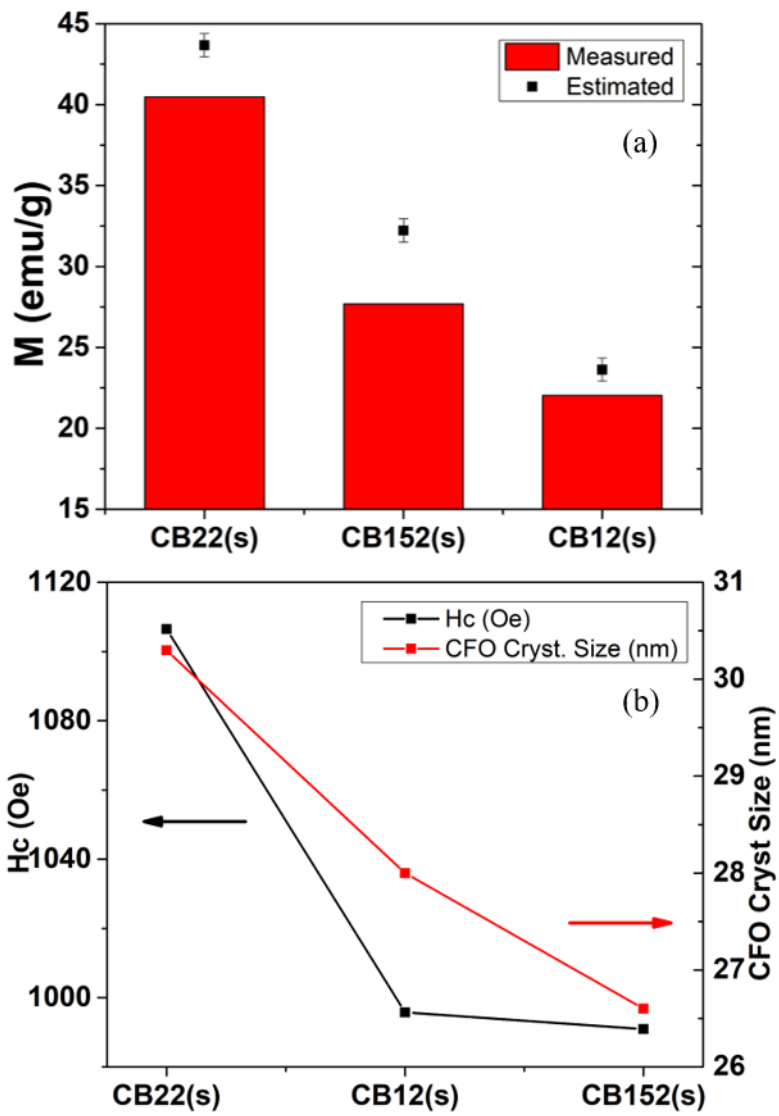
Figure 15. (a) Comparison of measured and estimated magnetization values and (b) relationship between CFO crystallite size and coercivity.

Table 4. Results of fitting to M−H loops. The FM and PM/AFM contributions are separated from the overall values. The asterisk (∗) indicates that the parameters were obtained by further calculations.

Sample	FM part				AFM/PM part		Combined*		
	M_s (emu/g)	Std. Error	H_c (Oe)	Std. Error	χ (emu/g.Oe)	Std. Error	M @ 20 kOe (emu/g)	M_r (emu/g)	H_c (Oe)
CFO	75.2	0.3	866	7	6.53E-05	1.83E-05	71.6	23.5	864
CB22(s)	40.5	0.3	1113	12	9.90E-05	1.53E-05	40.5	16.3	1106
CB152(s)	27.3	0.2	998	10	8.59E-05	8.91E-06	27.7	10.3	991
CB12(s)	22.1	0.1	1002	9	5.30E-05	6.72E-06	22.0	8.1	996

4.4. Electrical Properties

Figure 18 shows the electric polarization (P) versus electric field (E) curves (P–E loops) for the three different sintered samples, CB22(s), CB152(s), and CB12(s). The loops exhibit a distortion from an ideal ferroelectric behavior shown in bulk [65] and thin–film [66] BFO. Moreover, the loop shapes indicate the presence of conductor–like and leaky capacitor–like components in the samples [67]. This distortion can be attributed to two factors. First, the presence of non–ferroelectric CFO in the samples, increasing the contribution of the conductive component with CFO content (Figure 18), is similar to the cases observed in Ref. [23]. Second, the enhancement of crystal symmetry in the nano–sized BFO crystals results in a weaker ferroelectric behavior of BFO [68], as observed in sol–gel derived BFO [69]. The size–dependent ferroelectric behavior makes the distortion of P–E loops seem inevitable, even if the non–ferroelectric component is fully coated with a ferroelectric material [70]. Therefore, the best way to alleviate this issue is probably by doping the ferroelectric component in the nanocomposite in order to induce a stronger crystal asymmetry [71].

Despite such a deviation from ideal ferroelectric behavior, the

samples still showed the capability to store energy. To estimate the energy stored in the samples, we used Eq. (IV.2),

$$W_R = \int_{P_r}^{P_{max}} E\,dP \qquad\qquad (IV.2)$$

where W_R is the recoverable energy density, P_{max} is the maximum polarization, and P_r is the remnant polarization. We do note here that P_r is not the intrinsic remnant polarization of the ferroelectric component of the samples, due to the distortion caused by the leaky components [67]. From Eq. (IV.2), we estimated W_R = 0.08, 0.11, and 0.09 mJ/cm^3 for samples CB22(s), CB152(s), and CB12(s), respectively. However, considering the samples' leaky behavior, the stored energy may have been discharged in the form of leakage current.
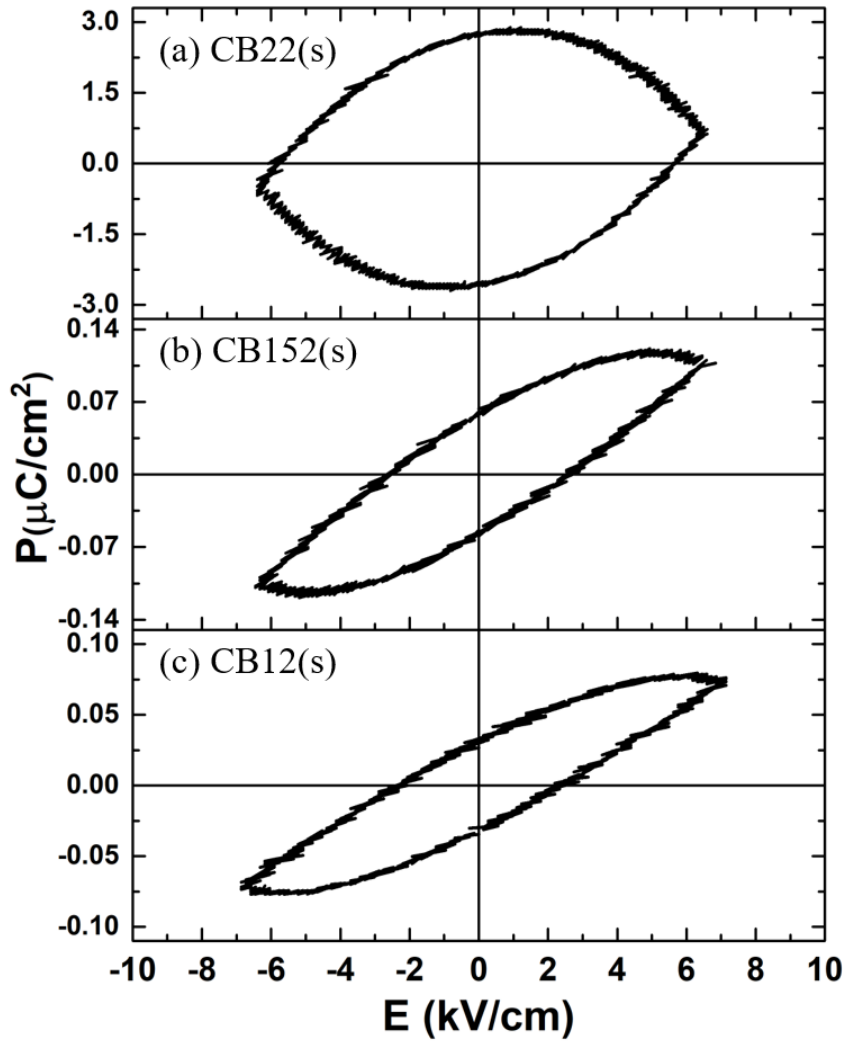
Figure 16. $P-E$ loops measured by poling to $\pm\sim$6.5 kV/cm at 12.5 Hz for sintered nanocomposite samples, (a) CB22(s), (b) CB152(s), and (c) CB12(s)

4.5. Magnetoelectric Properties

Figures 19 and 20 provide plots of the current density (J) and the polarization change (ΔP) as a function of the applied magnetic field (H), respectively. The $J-H$ plots in Figure 19 were obtained by removing the leakage current from the original $J-H$ plots shown in Figure 21(a). It was found from the Figure 19 plots that changes in current density are most prominent at fields lower than 20 kOe, which is within the range where CFO exhibits the strongest magnetostriction behavior [72]. Thus, the change in current density most likely originates from the strain transfer from magnetostrictive CFO to piezoelectric BFO, similarly to the emergence of ΔV reported in Ref. [24].

Figure 20 draws $\Delta P-H$ plots of the nanocomposites obtained by integrating the current density with respect to time (Figure 19). Here, ΔP represents [$P(H)-P(0$ kOe)] and the results for all the nanocomposites are summarized in Table 5. We note that sample CB22(s) exhibited the highest current density, followed by CB152(s) and CB12(s); consequently, CB22(s) possessed the largest value of $|\Delta P|$ = 295 $\mu C/m^2$ among our measurements. Such a large $|\Delta P|$ value of CB22(s) is of the same order of magnitude as that of single-

crystal BFO (~500 µC/m^2 at >100 kOe) [15], but is the largest achieved at a magnetic field as small as 20 kOe.

From Table 5, we can see that CB22(s) has the highest $|\Delta P|$ followed by CB152(s) and CB12(s). Two probable explanations for decreasing $|\Delta P|$ in this order are 1) the increase of BFO crystallite size and 2) the decrease of CFO content in the nanocomposites. Since $|\Delta P|$ most likely stems from a piezoelectric effect in BFO crystals, inverse size-dependence of piezoelectricity [73] can play a role in regulating the value of $|\Delta P|$ in nanocomposites. Consequently, smaller BFO crystals in CB22(s) can undergo a higher deformation rate and thus a higher piezoelectric effect compared to those in CB152(s) and CB12(s). Furthermore, the amount of CFO in CB152(s) and CB12(s) samples might be too low to impart a significant strain transfer to the BFO nanocrystals [24], thus resulting in lower $|\Delta P|$. The combination of these two factors might explain why $|\Delta P|$ is much lower for CB152(s) and CB12(s).

Comparing the polarization values in Figures 18 and 20, we notice that those obtained in applied magnetic fields (Figure 20) are two orders of magnitude lower than those obtained in applied electric fields (Figure 18). These discrepancies can be attributed to the

CFO–BFO structure in the nanocomposites. Under an applied electric field, all of the components of the nanocomposites are affected by the field and thus contribute to polarization. On the other hand, under an applied magnetic field, the polarization can occur only in BFO crystals that are in direct contact with CFO crystals. To alleviate this issue, one needs to engineer the CFO–BFO interface to form CFO cores covered with BFO shells so that all BFO can be strained upon the application of a magnetic field. In this regard, thin BFO shells would be beneficial to obtain an enhanced piezoelectric effect [73], yet one must keep in mind that this strategy may result in weaker ferroelectric behavior [68]. Furthermore, a more magnetostrictive material such as Terfenol–D [74] may be used to replace the CFO core and induce more strain to the BFO shell.

Lastly, we must be cautious in attributing the ΔP to magnetoelectric coupling, however, since the J–H relationship is invariant with respect to the sweep rate (Figure 23). For pure magnetoelectric coupling, ΔP can be calculated using Eq. (IV.3),

$$\Delta P = \frac{1}{dH/dt} \int_{H_{t=0}}^{H_{t=t}} J dH \qquad (\text{IV.3})$$

Since the amount of ΔP in a crystal is finite, an increase of dH/dt needs to be compensated by an increase of J. In our samples, it is

possible that positive magnetoresistance, unlike that reported in Ref. [75], hinders leakage current flow at high magnetic fields, allowing charge to migrate only at near-zero fields, and resulting in the formation of current-density peaks. On the other hand, it is also probable that a fast sweep rate means that current-density peaks appear when changes in leakage current are still large (Figure 20(b)), thus suppressing the significance of these peaks relative to the background data, with the result that the $\mathit{\Delta P}$ in Figure 24 varies with different sweep rates. This issue requires further studies for its clarification.
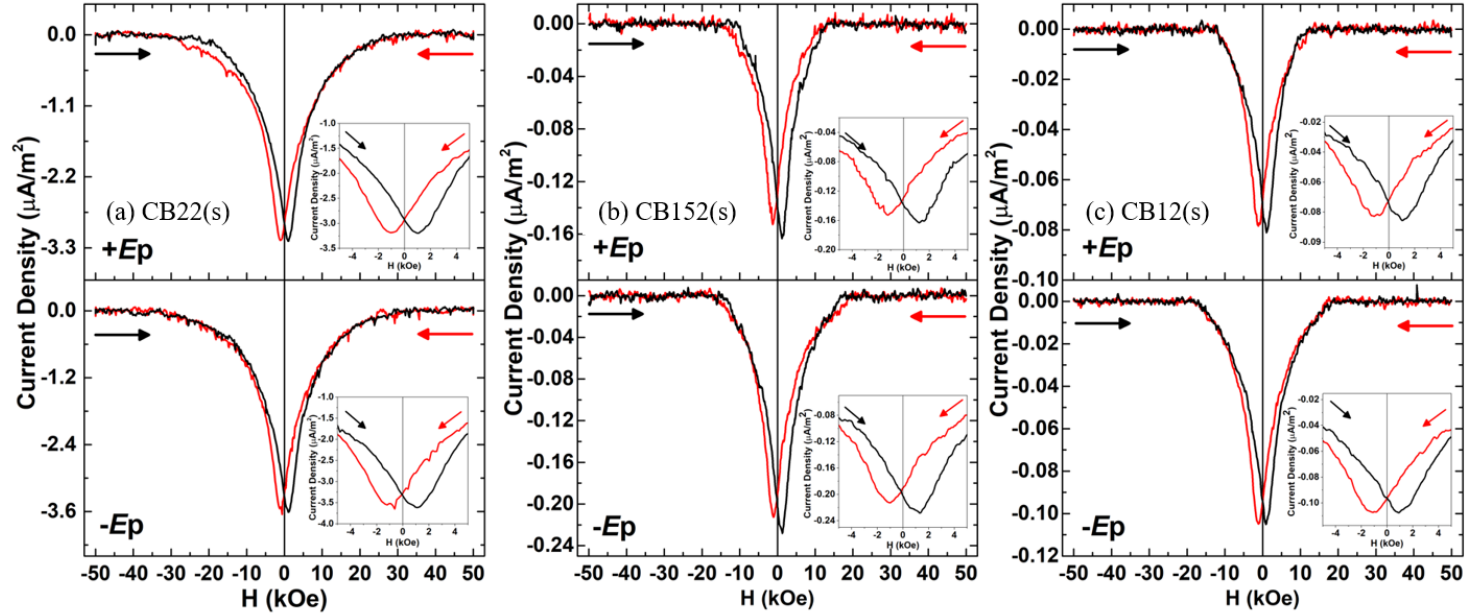
Figure 17. $J-H$ plots for sintered nanocomposite samples, (a) CB22(s), (b) CB152(s), and (c) CB12(s). The arrows indicate the magnetic-field sweeping direction, and the insets show the magnification of the current around the zero fields.
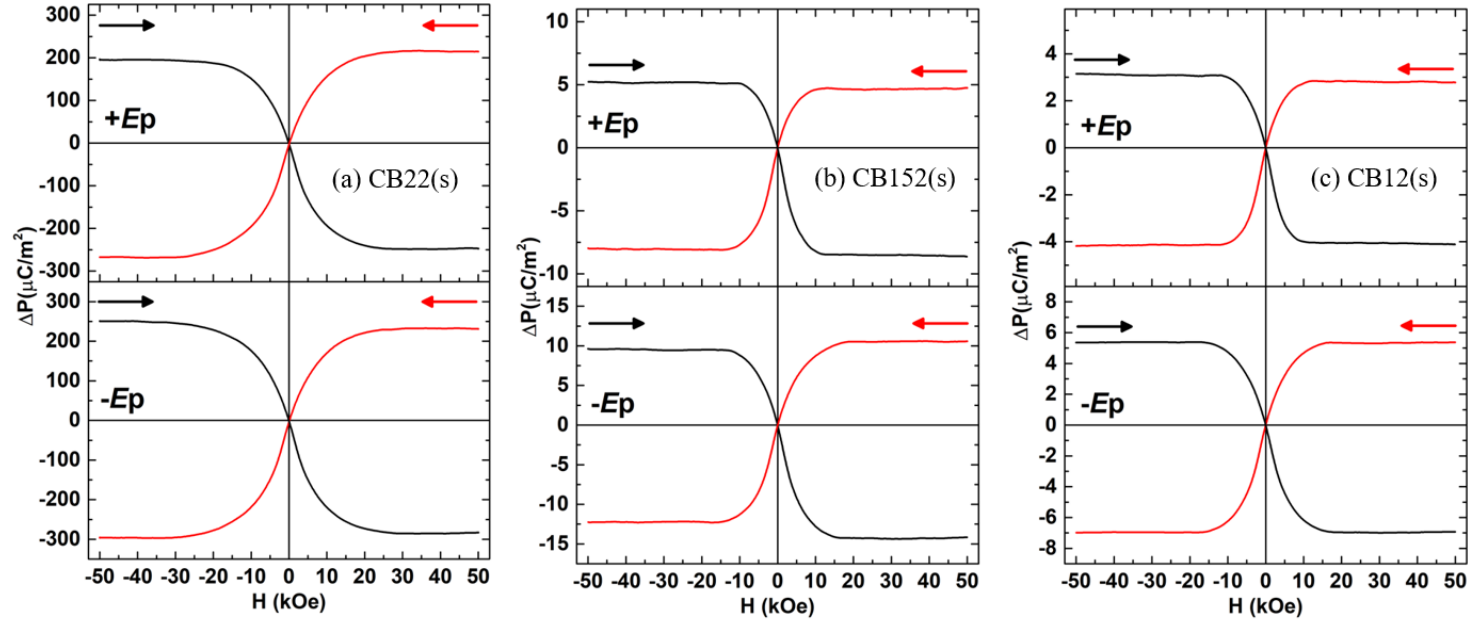
Figure 18. $\triangle P-H$ plots for sintered nanocomposite samples, (a) CB22(s), (b) CB152(s), and (c) CB12(s). The arrows indicate the magnetic−field sweeping direction.
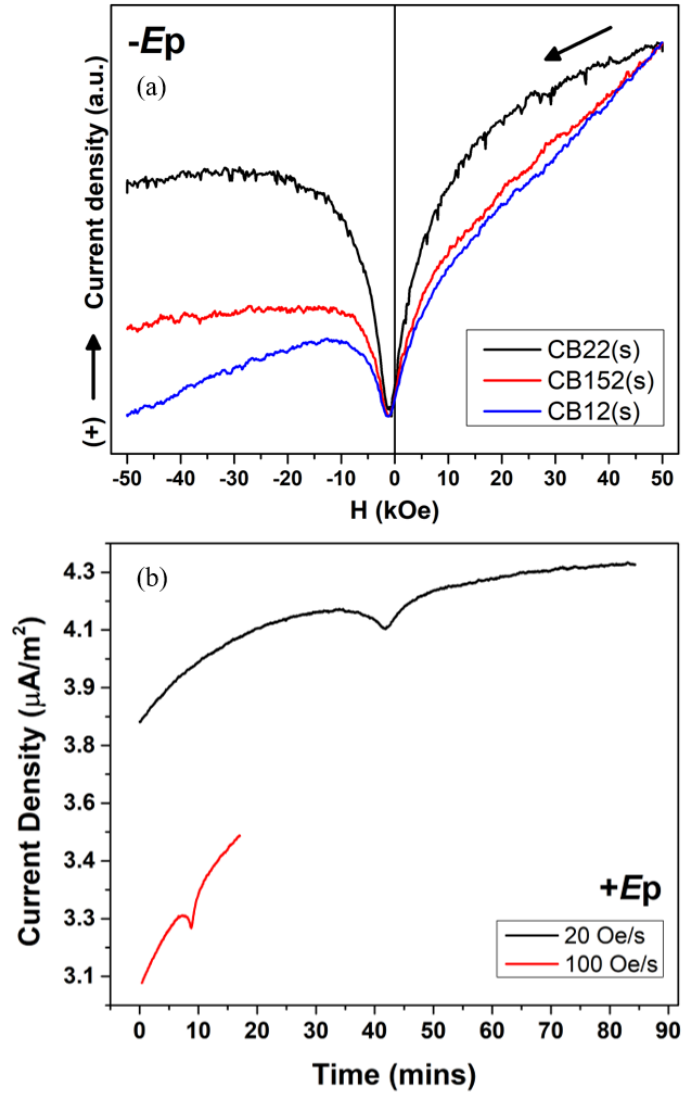
Figure 19. (a) As−measured *J−H* plots of sintered nanocomposites samples poled at −100V/ A steeper plot indicates a larger leakage current and (b) *J−*t plots of sample CB12(s). With the faster sweep rate, the current density peak appears when the current density change is still large.
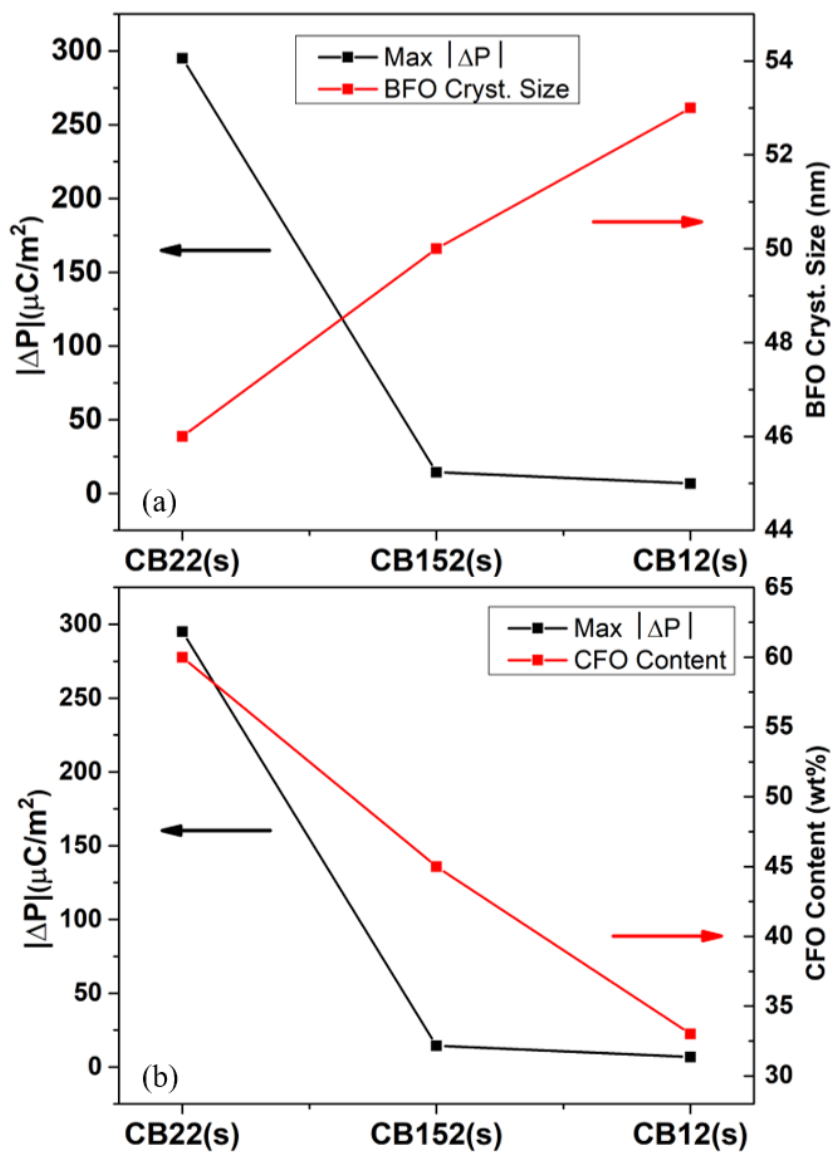
Figure 20. Relationship between max |△P| and (a) BFO crystallite

size and (b) CFO content.
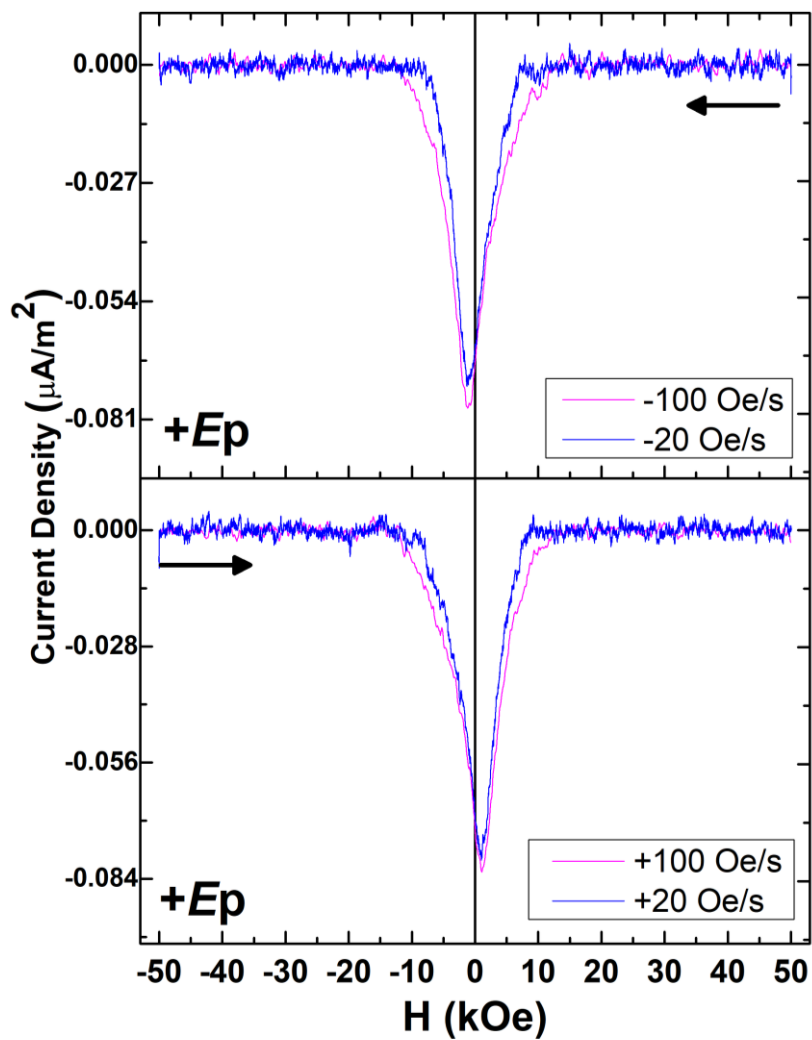
Figure 21. J−H plot of CB12(s) obtained from measurements with negative (top) and positive (bottom) scan rate
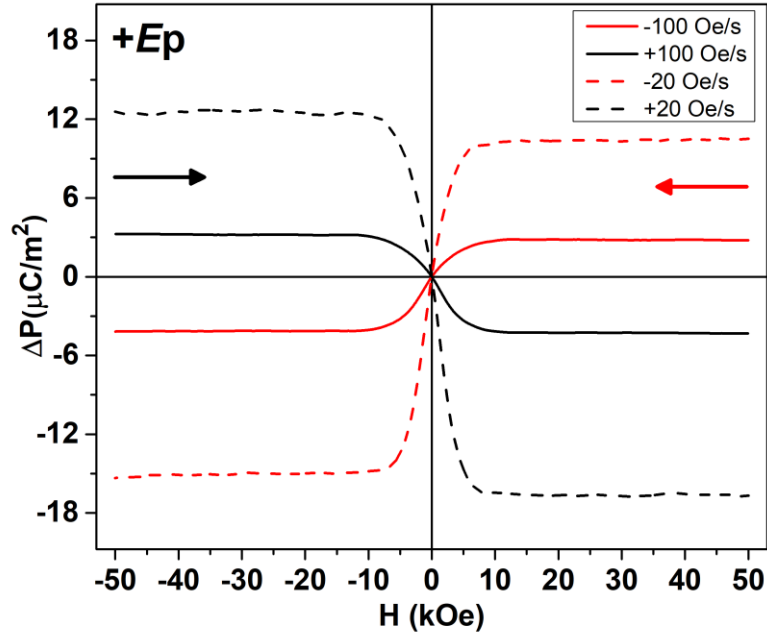
Figure 22. $\triangle P$−H plot of CB12(s) obtained from measurements with different scan rates.

Table 5. Summary of maximum |$\triangle$P| obtained from Figure 20.

| Sample | Maximum \|ΔP\| at ± 30 kOe (µC/m²) | | | |
| | +Ep | | -Ep | |
	(+) sweep	(-) sweep	(+) sweep	(-) sweep
CB22(s)	248	268	285	295
CB152(s)	8.3	7.6	14.4	12.2
CB12(s)	4.0	4.0	6.7	6.6

Chapter 5. Conclusions

In summary, our low−calcination−temperature synthesis methodology is favorable for high−purity CFO−BFO nanocomposites. Obtained TEM images show that CFO and BFO nanocrystals are inter−embedded in the nanocomposites. Magnetic characterizations indicate that the coercivities of the nanocomposites are higher than that of single−phase CFO, suggesting the presence of dipolar interaction between CFO and BFO in the ferrimagnetic nanocomposites, having magnetization values ranging from 22 to 41 emu/g at 20 kOe.

P−E loops show that the nanocomposites can store 0.09 to 0.11 mJ/cm^3 of energy and that the samples exhibited leaky behavior. We also estimated that a 30 kOe magnetic field can induce $|\Delta P|$ = 4.0 ~ 295 µC/m^2. Comparing the three nanocomposites, we found that the size of the BFO crystallites and the amount of CFO are crucial in order to establish significant electric polarization control by an applied magnetic field. This work offers an elaboration of the relationships among the synthesis, structure, and multiferroic properties of nanocomposites, which can be applied as design principles for a variety of multiferroic nanocomposite materials.

References

[1] M. Gajek, *et al.*, "Tunnel junctions with multiferroic barriers," *Nat. Mater.,* vol. 6, no. 4, pp. 296−302, 2007.

[2] J. Shen, *et al.*, "A multilevel nonvolatile magnetoelectric memory," *Sci. Rep.,* vol. 6, no. 1, pp. 34473, 2016.

[3] Y. Zhang, *et al.*, "Demonstration of magnetoelectric read head of multiferroic heterostructures," *Appl. Phys. Lett.,* vol. 92, no. 15, pp. 152510, 2008.

[4] F. Mushtaq, *et al.*, "Enhanced catalytic degradation of organic pollutants by multi−stimuli activated multiferroic nanoarchitectures," *Nano Res.,* vol. 13, no. 8, pp. 2183−2191, 2020.

[5] F. Mushtaq, *et al.*, "Magnetoelectrically Driven Catalytic Degradation of Organics," *Adv. Mater.,* vol. 31, no. 28, pp. 1901378, 2019.

[6] A. Rodzinski, *et al.*, "Targeted and controlled anticancer drug delivery and release with magnetoelectric nanoparticles," *Sci. Rep.,* vol. 6, no. 1, pp. 20867, 2016.

[7] M. Nair, *et al.*, "Externally controlled on−demand release of anti−HIV drug using magneto−electric nanoparticles as carriers," *Nat. Commun.,* vol. 4, no. 1, pp. 1707, 2013.

[8] S. Kiselev, "Detection of magnetic order in ferroelectric $BiFeO_3$ by neutron diffraction," *Sov. Phys.,* vol. 7, no., pp. 742, 1963.

[9] D. Lebeugle, *et al.*, "Room−temperature coexistence of large electric

polarization and magnetic order in BiFeO$_3$ single crystals," *Phys. Rev. B,* vol. 76, no. 2, pp. 024116, 2007.

[10]　M. Ramazanoglu*, et al.*, "Local weak ferromagnetism in single−crystalline ferroelectric BiFeO$_3$," *Phys. Rev. Lett.,* vol. 107, no. 20, pp. 207206, 2011.

[11]　A.K. Zvezdin, A.P. Pyatakov, "On the problem of coexistence of the weak ferromagnetism and the spin flexoelectricity in multiferroic bismuth ferrite," *EPL,* vol. 99, no. 5, pp. 57003, 2012.

[12]　I. Sosnowska, T.P. Neumaier, E. Steichele, "Spiral magnetic ordering in bismuth ferrite," *J. Phys. C,* vol. 15, no. 23, pp. 4835, 1982.

[13]　J.H. Lee, R.S. Fishman, "Giant Spin−Driven Ferroelectric Polarization in BiFeO$_3$ at Room Temperature," *Phys. Rev. Lett.,* vol. 115, no. 20, pp. 207203, 2015.

[14]　A.F. Popkov*, et al.*, "Origin of the giant linear magnetoelectric effect in perovskitelike multiferroic BiFeO$_3$," *Phys. Rev. B,* vol. 93, no. 9, pp. 094435, 2016.

[15]　M. Tokunaga*, et al.*, "Magnetic control of transverse electric polarization in BiFeO$_3$," *Nat. Commun.,* vol. 6, no. 1, pp. 5878, 2015.

[16]　D. Carranza−Celis*, et al.*, "Control of Multiferroic properties in BiFeO$_3$ nanoparticles," *Sci. Rep.,* vol. 9, no. 1, pp. 3182, 2019.

[17]　Y. Hu*, et al.*, "Synthesis of Bismuth Ferrite Nanoparticles via a Wet Chemical Route at Low Temperature," *J. Nanomater.,* vol. 2011, no., pp. 797639, 2011.

[18]   S.K.S. Patel, *et al.*, "Single−crystalline Gd−doped $BiFeO_3$ nanowires: R3c−to−Pn21a phase transition and enhancement in high−coercivity ferromagnetism," *J. Mater. Chem. C,* vol. 6, no. 3, pp. 526−534, 2018.

[19]   S.K.S. Patel, J.H. Lee, M.K. Kim, S.K. Kim, "Structural and Magnetic Properties of Gd−Ni−co−doped $BiFeO_3$ Nanoparticles," *J. Magn.,* vol. 24, no. 3, pp. 371−378, 2019.

[20]   D.V. Thang, N. Van Minh, "Magnetic Properties and Impedance Spectroscopic Studies of Multiferroic $Bi_{1-x}Nd_xFeO_3$ Materials," *J. Magn.,* vol. 21, no. 1, pp. 29−34, 2016.

[21]   I.Y. Khairani, *et al.*, "Fabrication, Structure, and Magnetic Properties of Pure−Phase $BiFeO_3$ and $MnFe_2O_4$ Nanoparticles and their Nanocomposites," *J. Magn.,* vol. 25, no. 2, pp. 140−149, 2020.

[22]   A. Das, *et al.*, "Magnetic, dielectric and magnetoelectric properties of $BiFeO_3$−$CoFe_2O_4$ nanocomposites," *J. Alloys Compd.,* vol. 697, no., pp. 353−360, 2017.

[23]   A. Khalid, *et al.*, "Magneto−electric coupling and multifunctionality in $BiFeO_3$−$CoFe_2O_4$ core−shell nano−composites," *Ceram. Int.,* vol. 46, no. 8, Part B, pp. 12828−12836, 2020.

[24]   S. Kuila, *et al.*, "Study of magnetization and magnetoelectricity in $CoFe_2O_4$/$BiFeO_3$ core−shell composites," *J. Appl. Phys.,* vol. 123, no. 6, pp. 064101, 2018.

[25]   M. Alam, S. Talukdar, K. Mandal, "Multiferroic properties of bilayered $BiFeO_3$/$CoFe_2O_4$ nano−hollowspheres," *Mater. Lett.,* vol. 210,

no., pp. 80−83, 2018.

[26]   B.D. Cullity, C.D. Graham, *Introduction to Magnetic Materials*, Reading: IEEE, 2008.

[27]   I. Dzyaloshinsky, "A thermodynamic theory of "weak" ferromagnetism of antiferromagnetics," *Journal of Physics and Chemistry of Solids,* vol. 4, no. 4, pp. 241−255, 1958.

[28]   T. Moriya, "Anisotropic Superexchange Interaction and Weak Ferromagnetism," *Phys. Rev.,* vol. 120, no. 1, pp. 91−98, 1960.

[29]   S. Kasap, Principles of electronic materials and devices, 2000,

[30]   W. Eerenstein, N.D. Mathur, J.F. Scott, "Multiferroic and magnetoelectric materials," *Nature,* vol. 442, no. 7104, pp. 759−765, 2006.

[31]   A. Van Run, D. Terrell, J. Scholing, "An in situ grown eutectic magnetoelectric composite material," *Journal of Materials Science,* vol. 9, no. 10, pp. 1710−1714, 1974.

[32]   J. Nie, G. Xu, Y. Yang, C. Cheng, "Strong magnetoelectric coupling in $CoFe_2O_4$−$BaTiO_3$ composites prepared by molten−salt synthesis method," *Materials Chemistry and Physics,* vol. 115, no. 1, pp. 400−403, 2009.

[33]   A. Chaudhuri, K. Mandal, "Large magnetoelectric properties in $CoFe_2O_4$:$BaTiO_3$ core−shell nanocomposites," *J. Magn. Magn. Mater.,* vol. 377, no., pp. 441−445, 2015.

[34]   P. Wang*, et al.*, "Colossal Magnetoelectric Effect in Core−Shell

Magnetoelectric Nanoparticles," *Nano Lett.,* vol. 20, no. 8, pp. 5765−5772, 2020.

[35]　　S. Fedulov, Determination of Curie temperature for the BiFeO₃ ferroelectric,　Dokl. Akad. Nauk, Russian Academy of Sciences, 1961, pp. 1345−1346

[36]　　M. Fiebig, T. Lottermoser, D. Meier, M. Trassin, "The evolution of multiferroics," *Nat. Rev. Mater.,* vol. 1, no. 8, pp. 16046, 2016.

[37]　　J. Wang*, et al.*, "Epitaxial BiFeO3 multiferroic thin film heterostructures," *Science,* vol. 299, no. 5613, pp. 1719−1722, 2003.

[38]　　A.M. Kadomtseva*, et al.*, "Phase transitions in multiferroic BiFeO3 crystals, thin−layers, and ceramics: enduring potential for a single phase, room−temperature magnetoelectric 'holy grail'," *Phase Transitions,* vol. 79, no. 12, pp. 1019−1042, 2006.

[39]　　A.K. Zvezdin, A.P. Pyatakov, "Flexomagnetoelectric effect in bismuth ferrite," *physica status solidi (b),* vol. 246, no. 8, pp. 1956−1960, 2009.

[40]　　F. Keffer, "Moriya Interaction and the Problem of the Spin Arrangements in β MnS," *Phys. Rev.,* vol. 126, no. 3, pp. 896, 1962.

[41]　　A. Moskvin, I. Bostrem, "Some Peculiarities of Exchange Interactions in Orthoferrite−Orthochromites," *Физика твердого тела,* vol. 19, no. 9, pp. 1616−1626, 1977.

[42]　　R. Chen, M.G. Christiansen, P. Anikeeva, "Maximizing Hysteretic Losses in Magnetic Ferrite Nanoparticles via Model−Driven Synthesis

and Materials Optimization," *ACS Nano,* vol. 7, no. 10, pp. 8990−9000, 2013.

[43]   C. Friderichs, N. Zotov, W. Mader, "Synthesis of Monodisperse SrTi1-xZrxO3 Nanocubes in Oleate by a Two−Phase Solvothermal Method," *Eur. J. of Inorg. Chem.,* vol. 2015, no. 2, pp. 288−295, 2015.

[44]   C. Zhang*, et al.,* "Room temperature exchange bias in multiferroic BiFeO3 nano− and microcrystals with antiferromagnetic core and two− dimensional diluted antiferromagnetic shell," *J. Nanopart. Res.,* vol. 19, no. 5, pp. 182, 2017.

[45]   T. Hyeon, "Chemical synthesis of magnetic nanoparticles," *Chemical Communications,* vol., no. 8, pp. 927−934, 2003.

[46]   J. Park*, et al.,* "Ultra−large−scale syntheses of monodisperse nanocrystals," *Nat. Mater.,* vol. 3, no. 12, pp. 891−895, 2004.

[47]   D. Caruntu*, et al.,* "Solvothermal synthesis and controlled self− assembly of monodisperse titanium−based perovskite colloidal nanocrystals," *Nanoscale,* vol. 7, no. 30, pp. 12955−12969, 2015.

[48]   T. Tong*, et al.,* "Controllable phase evolution of bismuth ferrite oxides by an organic additive modified hydrothermal method," *Ceram. Int.,* vol. 41, no., pp. S106−S110, 2015.

[49]   D. Cai*, et al.,* "Phase evolution of bismuth ferrites in the process of hydrothermal reaction," *Materials Chemistry and Physics,* vol. 134, no. 1, pp. 139−144, 2012.

[50]   S. Ghosh, S. Dasgupta, A. Sen, H. Sekhar Maiti, "Low−Temperature

Synthesis of Nanosized Bismuth Ferrite by Soft Chemical Route," *J. Am. Ceram. Soc.,* vol. 88, no. 5, pp. 1349−1352, 2005.

[51]   L. Lutterotti, D. Chateigner, S. Ferrari, J. Ricote, "Texture, residual stress and structural analysis of thin films using a combined X−ray analysis," *Thin Solid Films,* vol. 450, no. 1, pp. 34−41, 2004.

[52]   C.B. Sawyer, C.H. Tower, "Rochelle Salt as a Dielectric," *Phys. Rev.,* vol. 35, no. 3, pp. 269−273, 1930.

[53]   L.H. Yin*, et al.,* "Pressure−induced ferroelectricity and enhancement of Mn−Mn exchange striction in $GdMn_2O_5$," *J. Appl. Phys.,* vol. 119, no. 10, pp. 104101, 2016.

[54]   N. Sheoran, V. Kumar, A. Kumar, "Comparative study of structural, magnetic and dielectric properties of $CoFe_2O_4@BiFeO_3$ and $BiFeO_3@CoFe_2O_4$ core−shell nanocomposites," *J. Magn. Magn. Mater.,* vol. 475, no., pp. 30−37, 2019.

[55]   H. Han, J.H. Lee, H.M. Jang, "Low−Temperature Solid−State Synthesis of High−Purity $BiFeO_3$ Ceramic for Ferroic Thin−Film Deposition," *Inorg. Chem.,* vol. 56, no. 19, pp. 11911−11916, 2017.

[56]   L.S. Ferreira*, et al.,* "Structure, magnetic behavior and OER activity of $CoFe_2O_4$ powders obtained using agar−agar from red seaweed (Rhodophyta)," *Materials Chemistry and Physics,* vol. 237, no., pp. 121847, 2019.

[57]   A.A. Sattar, H.M. El−Sayed, I. Alsuqia, "Structural and magnetic properties of $CoFe_2O_4/NiFe_2O_4$ core/shell nanocomposite prepared by

the hydrothermal method," *J. Magn. Magn. Mater.,* vol. 395, no., pp. 89-96, 2015.

[58]   M.B. Stearns, Y. Cheng, "Determination of para- and ferromagnetic components of magnetization and magnetoresistance of granular Co/Ag films (invited)," *J. Appl. Phys.,* vol. 75, no. 10, pp. 6894-6899, 1994.

[59]   V. Singh*, et al.,* "Effect of polymer coating on the magnetic properties of oxygen-stabilized nickel nanoparticles," *Phys. Rev. B,* vol. 82, no. 5, pp. 054417, 2010.

[60]   A. Franco, F.L.A. Machado, V.S. Zapf, "Magnetic properties of nanoparticles of cobalt ferrite at high magnetic field," *J. Appl. Phys.,* vol. 110, no. 5, pp. 053913, 2011.

[61]   Y. Huang*, et al.,* "Strong room temperature spontaneous exchange bias in $BiFeO_3-CoFe_2O_4$ nanocomposites," *J. Alloys Compd.,* vol. 762, no., pp. 438-443, 2018.

[62]   J. Nogués*, et al.,* "Exchange bias in nanostructures," *Phys. Rep.,* vol. 422, no. 3, pp. 65-117, 2005.

[63]   P.T. Phong*, et al.,* "Size-controlled heating ability of $CoFe_2O_4$ nanoparticles for hyperthermia applications," *Phys. B,* vol. 531, no., pp. 30-34, 2018.

[64]   P. Jeppson*, et al.,* "Cobalt ferrite nanoparticles: Achieving the superparamagnetic limit by chemical reduction," *J. Appl. Phys.,* vol. 100, no. 11, pp. 114324, 2006.

[65]   W.N. Su*, et al.,* "Large polarization and enhanced magnetic

properties in BiFeO$_3$ ceramic prepared by high-pressure synthesis," *Appl. Phys. Lett.,* vol. 91, no. 9, pp. 092905, 2007.

[66]   M. Liu*, et al.,* "Energy Storage Characteristics of BiFeO$_3$ /BaTiO$_3$ Bi-Layers Integrated on Si," *Materials (Basel),* vol. 9, no. 11, pp. 935, 2016.

[67]   M. Fukunaga, Y. Noda, "New Technique for Measuring Ferroelectric and Antiferroelectric Hysteresis Loops," *J. Phys. Soc. Jpn.,* vol. 77, no. 6, pp. 064706, 2008.

[68]   S.M. Selbach, T. Tybell, M.-A. Einarsrud, T. Grande, "Size-Dependent Properties of Multiferroic BiFeO$_3$ Nanoparticles," *Chem. Mater.,* vol. 19, no. 26, pp. 6478-6484, 2007.

[69]   M. Kumar, K.L. Yadav, G.D. Varma, "Large magnetization and weak polarization in sol-gel derived BiFeO$_3$ ceramics," *Mater. Lett.,* vol. 62, no. 8, pp. 1159-1161, 2008.

[70]   K. Shahzad*, et al.,* "Field-controlled magnetoelectric core-shell CoFe$_2$O$_4$@BaTiO$_3$ nanoparticles as effective drug carriers and drug release in vitro," *Materials Science and Engineering: C,* vol. 119, no., pp. 111444, 2021.

[71]   H. Yabuta*, et al.,* "Enhancement of tetragonal anisotropy and stabilisation of the tetragonal phase by Bi/Mn-double-doping in BaTiO$_3$ ferroelectric ceramics," *Sci. Rep.,* vol. 7, no. 1, pp. 45842, 2017.

[72]   K.K. Mohaideen, P.A. Joy, "Enhancement in the Magnetostriction of Sintered Cobalt Ferrite by Making Self-Composites from

Nanocrystalline and Bulk Powders," *ACS Appl. Mater. Interfaces,* vol. 4, no. 12, pp. 6421−6425, 2012.

[73]   S.−D. Kim*, et al.,* "Inverse size−dependence of piezoelectricity in single BaTiO$_3$ nanoparticles," *Nano Energy,* vol. 58, no., pp. 78−84, 2019.

[74]   S.H. Lim*, et al.,* "Magnetostrictive properties of polymer−bonded Terfenol−D composites," *J. Magn. Magn. Mater.,* vol. 191, no. 1, pp. 113−121, 1999.

[75]   S. Kuila*, et al.,* "Magnetoresistance in CoFe$_2$O$_4$/BiFeO$_3$ core−shell nanoparticles near room temperature," *J. Appl. Phys.,* vol. 124, no. 15, pp. 154104, 2018.

초록

서로 다른 세 가지의 몰 비율 (CFO:BFO = 2:2, 1.5:2, and 1:2)로 이루어진 $CoFe_2O_4-BiFeO_3$ (CFO-BFO) 나노복합소재를 열수/시트르산 솔-젤이 복합된 방법을 이용하여 합성했습니다. 이 방법론으로 고순도의 결정질 나노복합소재를 450℃ 의 낮은 하소 온도에서 합성했습니다. 투과전자현미경(TEM) 이미지를 통해 CFO와 BFO 나노결정들은 서로 섞여있다는 것을 알 수 있었습니다. 2:2의 비율로 소결된 샘플의 자기적 특성은 상온에서 자기장이 20 kOe로 가해질 때 40.7 emu/g의 높은 자화값을 나타냈습니다. 자화값과 보자력값은 CFO와 BFO의 스핀이 교환 상호작용하고 있다는 것을 나타냈습니다. 분극-전기장($P-E$) 루프 측정결과는 모든 샘플에서 전류가 누설되는 거동을 보임에도 불구하고, 상온에서 자기장이 ~30 kOe로 가해질 때 전기 분극 변화량 (ΔP) 은 ~295 $\mu C/m^2$ 로 예상되었습니다. 제시된 이 결과들은 고순도의 다강체 CFO-BFO 나노복합소재의 전기적 분극을 자기장으로 조절할 수 있는 신뢰할만한 방법을 보여줬습니다.

Acknowledgments

I would like to thank my thesis advisor, Prof. Sang-Koog Kim for his time and effort in guiding me throughout my master's degree studies. Not only that he supports my research intellectually and financially, he also dedicates some of his time to help me achieve my career goals.

I would also like to express my gratitude to all members of the Research Center for Spin-Wave and Spin Dynamics (ReC-SDSW), specifically, Dr. Biswanath Bhoi, Dr. Shatabda Bhattacharya, Bosung Kim, Jaehak Yang, Jae Hyeok Lee, Haechan Jeon, Yongsub Kim, Jaegun Sim, Hyeon-Kyu Park, Gyu Young Park, Inna Yusnila Khairani, Trivoramai Jilalerspong, Loic Millet, Jiyeol Yoon, Ahn Hyeon, Seung-hoon Jang and Yeonjoo Oh for their help and encouragement during my studies. Without them, my life as a graduate student would be unbearable.

Additionally, I would like to appreciate the help from Prof. Kee Hoon Kim, Dr. Chang Bae Park, and Kwang-Tak Kim for their help in the electrical and mangnetoelectric property measurements. Furthermore, I would like to thank the staff at the Research Institute of Advanced Materials for their help in materials characterizations.

72

Finally, I am grateful to have a loving family back in Indonesia and friends in Korea. Their endless support gave me more confidence and motivation to keep pushing and eventually obtain my master's degree.